ErbB dysregulation impairs cognition via myelination-dependent and -independent oligodendropathy

Authors

Xu Hu,[1,4] Guanxiu Xiao,[1,4] Li He,[1,4] Qingyu Zhu,[1] Xiaojie Niu,[1] Huashun Li,[1] Qi Xu,[1] Zhengdong Wei,[1] Hao Huang,[1] Yifei Luan,[1] Mengsheng Qiu,[1] Kenji F. Tanaka,[2] Ying Shen,[3] and Yanmei Tao[1,*]

Affiliations

[1]Key Lab of Organ Development and Regeneration of Zhejiang Province, Institute of Life Sciences, College of Life and Environmental Sciences, Hangzhou Normal University, Hangzhou 311121, China.

[2]Department of Neuropsychiatry, Keio University School of Medicine, Tokyo 160-8582, Japan.

[3]Department of Neurobiology, Key Laboratory of Medical Neurobiology of Zhejiang Province, Zhejiang University School of Medicine, Hangzhou 310058, China.

[4]These authors contribute equally.

[*]Correspondence: ytao@hznu.edu.cn

Abstract

White matter abnormalities are an emerging pathological feature of schizophrenia. However, their attributions to the disease remain largely elusive. ErbB receptors and their ligands, some of which are essential for peripheral myelination, confer susceptibility to schizophrenia. By synergistically manipulating ErbB receptor activities in a oligodendrocyte-stage-specific manner in mice after early development, we demonstrate the distinct effects of ErbB signaling on oligodendrocytes at various differentiation states. ErbB overactivation, in mature oligodendrocytes, induces necroptosis causing demyelination, whereas in oligodendrocyte precursor cells, induces apoptosis causing hypomyelination. In contrast, ErbB inhibition increases oligodendrocyte precursor cell proliferation but induces hypomyelination by suppressing the myelinating capabilities of newly-formed oligodendrocytes. Remarkably, ErbB inhibition in mature oligodendrocytes diminishes axonal conduction under energy stress and impairs working memory capacity independently of myelin pathology. This study reveals the etiological implications of oligodendrocyte vulnerability induced by ErbB dysregulation, and elucidates the pathogenetic mechanisms for variable structural and functional white matter abnormalities.

Introduction

Adolescence is the critical period for the central nervous system (CNS) to completely develop and mature. In particular, CNS myelin generated by oligodendrocytes (OLs) is one of the most developmentally active component in the adolescent brain. This may lead to CNS myelin being a highly susceptible target in psychiatric disorders such as schizophrenia which typically develops during adolescence (*Fields, 2008; Hoistad et al., 2009; Kessler et al., 2007; Peters and Karlsgodt, 2015*). A growing body of literature points to abnormalities in the structure, component proteins, or regulating molecules of CNS myelin in schizophrenic patients (*Douaud et al., 2007; Fields, 2008; Hof and Schmitz, 2009; Hoistad et al., 2009; Kelly et al., 2018; Uranova et al., 2011*). Schizophrenia is increasingly viewed as a spectrum disorder based on varied symptom severity and genetic risk. Especially, white-matter microstructural changes as examined by structural brain imaging techniques are sensitive to the symptom severity or genetic loading of schizophrenic patients (*Karlsgodt, 2020*). Therefore, understanding schizophrenia related myelin pathogenesis is crucial for the development of diagnostic standards or therapeutic targets given that it is one of the most promising features whose progression can be examined periodically in patients.

Tyrosine kinase receptors ErbB(1-4) mediate the signaling of numerous growth factors which are categorized into the neuregulin (NRG) family and the epidermal growth factor (EGF) family (*Iwakura and Nawa, 2013; Mei and Nave, 2014*). The NRG and EGF family members bind differentially to the four ErbB receptors. Due to the indispensable function of NRG1-ErbB signaling in peripheral myelination (*Nave and Salzer, 2006*), it was expected that NRG-ErbB signaling played a role in CNS myelin development. However, the contradictory results from different research

groups have silenced any significance of this previous postulate (*Brinkmann et al., 2008; Makinodan et al., 2012; Schmucker et al., 2003; Taveggia et al., 2008*). Genetic ablation of *NRG1* or *ErbB4*, the ligand and receptor that have received extensive attention from researchers in schizophrenia field (*Harrison and Law, 2006; Mei and Nave, 2014*), induces neither developmental alteration nor pathogenesis in white matter of mutant mice (*Brinkmann et al., 2008*). However, studies combining genetic linkage analysis and brain imaging techniques have associated *NRG1* or *ERBB4* variability with reduced white matter density or integrity in human subjects (*McIntosh et al., 2008; Winterer et al., 2008; Zuliani et al., 2011*).

Notably, in addition to NRG1 and ErbB4, many molecules in the ErbB signaling pathways exhibit single nucleotide polymorphisms (SNPs) or aberrant expression that are implicated in schizophrenia or other psychiatric disorders. Both gain and loss of ErbB signaling have been indicated by genetic and biochemical studies (*Harrison and Law, 2006; Mei and Nave, 2014*). Particularly, NRG1 and ErbB4 have been revealed to increase the mRNA levels, protein levels, or receptor activity in the schizophrenic brain (*Chong et al., 2008; Hahn et al., 2006; Joshi et al., 2014; Law et al., 2006; Law et al., 2012*). It is noteworthy that EGFR (ErbB1), which only binds the EGF family ligands, is elevated in the brain of schizophrenic patients (*Futamura et al., 2002*) and shows potential in regulating oligodendrogenesis in developmental and pathological conditions (*Aguirre et al., 2007*). Thus, NRG-ErbB and EGF-ErbB signaling may be synergistic in the regulation of CNS myelin integrity.

In the CNS, OL precursor cells (OPCs) after terminal mitosis differentiate into newly-formed OLs (NFOs). NFOs then span differentiation states from pre-myelinating OLs to newly myelinating OLs. Myelinating OLs effectively generate myelin sheaths in a short time window before further differentiating into mature OLs

(MOs) that maintain the myelin sheath (*Bergles and Richardson, 2015; Czopka et al., 2013; Hughes et al., 2018; Tripathi et al., 2017; Watkins et al., 2008; Xiao et al., 2016*). To study whether ErbB receptors, through mediating NRG-ErbB and EGF-ErbB signaling, cooperate to regulate OLs and CNS myelin, we adopted an inducible pan-ErbB strategy and manipulated ErbB receptor activities specifically in OL lineage cells *in vivo*. This strategy allowed us to avoid characterizing the complex composition of ErbB ligands or receptors in OL lineage cells and helped us focus on their cellular function. The results reveal that ErbB dysregulation differentially affects OPCs, NFOs, and MOs, leading to CNS demyelination, hypomyelination, and even OL dysfunction that causes cognitive deficits independently of myelin pathology.

Results

ErbB overactivation in OLs induces demyelination and hypomyelination

Studies on OL-specific knock-out mice have validated the expression of ErbB3 and ErbB4 in OLs (*Brinkmann et al., 2008*), while phosphorylated EGFR is detected in OLs by immunostaining (*Palazuelos et al., 2014*). We characterized the expression of ErbB receptor members in subcortical white matter regions at different postnatal days. Note that the subcortical white matter regions isolated from mice before P5 had few myelin components. Our results indicate that ErbB2 is barely expressed in mouse CNS myelin, whereas EGFR, ErbB3 and ErbB4 are expressed with relatively stable levels during juvenile to adolescent development (Figure 1-figure supplement 1A,B).

To manipulate ErbB receptor activities in the OL lineage of mice, we employed tetracycline-controlled systems whose induction or blockade depends on the presence of doxycycline (Dox). We first characterized the impact of elevated ErbB receptor activities on CNS myelin by generation of *Plp*-tTA;*TRE*-ErbB2^{V664E} (*Plp*-ErbB2^{V664E}) bi-transgenic 'Tet-Off' mice (Figure 1A). Notably, *Plp*-ErbB2^{V664E} mice around P35 exhibited severe ataxia while walking on a grid panel (Figure 1B). Moreover, *Plp*-ErbB2^{V664E} mice showed difficulty in rolling over, indicating severely impaired motor coordination.

With the expression and phosphorylation of ectopic ErbB2^{V664E}, endogenous ErbB receptors (EGFR, ErbB3 and ErbB4) were strikingly phosphorylated and activated in the white matter of *Plp*-ErbB2^{V664E} mice (Figure 1C,D). Overactivation of ErbB receptors caused lower myelin staining intensity as exhibited in the corpus callosum of *Plp*-ErbB2^{V664E} mice at 9 days post Dox-withdrawal (dpd) after LFB staining. Notably, at 14 dpd, myelin loss became more evident throughout the corpus callosum, suggesting that *Plp*-ErbB2^{V664E} mice were undergoing CNS demyelination after Dox withdrawal (Figure 1E,F). Consistently, western blotting revealed loss of myelin basic protein (MBP), an indicator for MOs and myelin, in the brain of *Plp*-ErbB2^{V664E} mice (Figure 1G). Moreover, the electron microscopic examination (EM) of the myelin ultrastructure revealed that myelin sheaths of some axons in *Plp*-ErbB2^{V664E} mice ruptured or underwent breakdown (Figure 1H,I and Figure 1-figure supplement 2A), consistent with the idea of demyelination. Due to demyelination, only a few intact axons were detected in the midline of the corpus callosum of *Plp*-ErbB2^{V664E} mice at 14 dpd (Figure 1H,I). When axonal tracts in the corpus callosum were immunostained by TuJ1, the antibody recognizing neuronal specific β-tubulin III, the immunoreactivity dramatically reduced in *Plp*-ErbB2^{V664E} mice at 14 dpd (Figure

1-figure supplement 2B). In addition, as a pathological condition, demyelination is usually complicated and aggravated by the pathological responses from nearby astrocytes and microglia. Indeed, in the white matter of *Plp*-ErbB2^{V664E} mice, astrogliosis and microgliosis were revealed (Figure 1J,K).

Interestingly, despite the demyelination, the detectable axons, throughout the corpus callosum, optic nerve, and prefrontal cortex in *Plp*-ErbB2^{V664E} mice, were hypermyelinated. Myelinated axons detected in the brain of *Plp*-ErbB2^{V664E} mice had significantly smaller *g*-ratio (axon diameter/fiber diameter), a quantitative indication of myelin thickness for individual axons with different diameters (Figure 1I). Myelin thickness showed no difference between *TRE*-ErbB2^{V664E} and littermate *Plp*-tTA mice after Dox withdrawal (Figure 1-figure supplement 2C). Therefore, hypermyelination of detectable axons in *Plp*-ErbB2^{V664E} mice was a result of the overexpression of ErbB2^{V664E}, which was detected by an antibody against ErbB2 (Figure 1C,G).

Hypermyelination of individual axons in *Plp*-ErbB2^{V664E} mice phenocopied that observed in NRG1-overexpressing mice (*Brinkmann et al., 2008*). Notably, EM examination of the ultrastructure in *Plp*-ErbB2^{V664E} mice at 9 dpd revealed that most axons were intact in the midline of the corpus callosum, although they have been significantly hypermyelinated (Figure 1-figure supplement 2D,E). These results confirmed that hypermyelination occurs early in *Plp*-ErbB2^{V664E} mice, and demyelination and axonal degeneration in *Plp*-ErbB2^{V664E} mice are pathological events induced secondarily by continuous ErbB activation.

Next, we examined the effects of ErbB activation on CNS myelin by a 'Tet-on' system generated in *Sox10*$^{+/rtTA}$;*TRE*-ErbB2^{V664E} (*Sox10*-ErbB2^{V664E}) mice (Figure 1L). *Sox10*-ErbB2^{V664E} mice with Dox feeding from P21 developed severe motor

dysfunction, including ataxia and tremors, and died around P35. As a result, *Sox10*-ErbB2^{V664E} and littermate control mice were investigated at P30 after 9 days with Dox-feeding (dwd). These mice had smaller body sizes at P30 and walked with difficulty on a grid panel (Figure 1M). Western blotting revealed the expression and phosphorylation of ectopic ErbB2^{V664E} accompanied with increases in phosphorylation of ErbB3 and ErbB4, but not that of EGFR, in the white matter of *Sox10*-ErbB2^{V664E} mice (Figure 1N,O). Brain slices stained by LFB exhibited lower staining intensity in the white matter of *Sox10*-ErbB2^{V664E} mice (Figure 1P,Q), consistent with the lower MBP levels detected by western blotting (Figure 1N,O). The examination of the ultrastructure by EM revealed that the axons in the corpus callosum and optic nerve of *Sox10*-ErbB2^{V664E} mice exhibited thinner myelin with significantly increased *g*-ratio (Figure 1S). *Sox10*$^{+/rtTA}$ is a knock-in mouse line, so that the allele with *Sox10*-rtTA would not transcribe *Sox10* mRNA (*Ludwig et al., 2004*). We analyzed the ultrastructure of myelinated axons in *Sox10*$^{+/rtTA}$ and littermate *TRE*-ErbB2^{V664E} mice at P30 and did not observe any differences (Figure 1-figure supplement 2F), therefore we can exclude the possible effect of haploinsufficiency of Sox10 on late postnatal myelin development.

It is notable that in *Sox10*-ErbB2^{V664E} mice, the numbers of myelinated axons were not altered (Figure 1R), and myelin sheaths exhibited normal morphology (Figure 1S). Moreover, neither microgliosis nor astrogliosis was detected in the white matter of *Sox10*-ErbB2^{V664E} mice (Figure 1T,U). Because there was no indication of inflammatory pathogenesis, we can conclude that thinner myelin in *Sox10*-ErbB2^{V664E} white matter are caused by developmental deficits not pathological conditions. Therefore, ErbB activation in *Sox10*-ErbB2^{V664E} mice induces CNS hypomyelination rather than demyelination.

***Plp*-tTA targets mainly MOs whereas *Sox10*$^{+/rtTA}$ targets OPC-NFOs**

The finding that *Plp*-ErbB2^{V664E} and *Sox10*-ErbB2^{V664E} mice had no overlaps in histological and biochemical phenotypes was unexpected considering that Sox10 is reported to express throughout the OL lineage, and *Sox10*$^{+/rtTA}$ knock-in mice have been used to investigate all OL lineage cells (*Wegener et al., 2015*). Because the induction of the 'Tet-on' or 'Tet-off' system by Dox feeding or Dox withdrawal has a delayed effect on gene expression, and reporter proteins could accumulate to label the consecutive cellular stages, the results obtained by using *TRE*-controlled reporter mice fail to accurately reveal the original cells targeted by tTA or rtTA. To circumvent this problem, we delivered a *TRE*-controlled fluorescence reporter carried by an adeno-associated virus (AAV) into the mouse brains at P14 or P35, and examined tTA- or rtTA-targeted cells as well as their derivatives within 2 days.

Plp-tTA mice were raised with no Dox feeding, whereas *Sox10*$^{+/rtTA}$ were fed with Dox for 3 days before the stereotactic injection (Figure 2A). One or 2 days after virus injection, the reporter-expressing (YFP^{+}) cells were all immunopositive for Olig2 in both mouse lines at either age (Figure 2-figure supplement 1A-D), confirming their OL lineage specificity. To analyze the differentiation stage specificity, we immunostained AAV-*TRE*-YFP infected brain slices with an antibody for NG2 or PDGFRα that labels OPCs, or the antibody CC1 that labels post-mitotic OLs. The results showed that very few (4-7%) YFP^{+} cells were OPCs, while 92-97% of them were post-mitotic OLs 1 or 2 days after virus injection in *Plp*-tTA mice at either age, as well as in *Sox10*$^{+/rtTA}$ mice at P14 (Figure 2B,C and Figure 2-figure supplement 1A-D). However, for *Sox10*$^{+/rtTA}$ mice at P35, approximately 26% of

YFP$^+$ cells were OPCs 1 day after virus injection, and it decreased to 8% after 1 more day (Figure 2C). It is known that OPCs can differentiate into NFOs as quick as 2.5 hours (*Xiao et al., 2016*). These results may suggest that most OPCs targeted by *Sox10*-rtTA at P35 are undergoing terminal differentiation (tOPCs), and *Sox10*-rtTA increasingly targets tOPCs from P14 to P35.

There are also OL lineage cells belonging to the NFO stage that includes a transition from CC1$^-$ to CC1$^+$. β-catenin effector TCF4 is specifically expressed in the NFO stage (*Fancy et al., 2009; Fu et al., 2009; Ye et al., 2009*), which is present in a subset of Olig2$^+$ cells but is absent in OPCs (PDGFRα$^+$) in mice at P30 (Figure 2D). In *Sox10*$^{+/rtTA}$ mice at P14, immunostaining revealed that approximately 49% of YFP$^+$ cells were NFOs (TCF4$^+$) 1 day after virus injection, but it reduced to 28% after 1 more day (Figure 2E,G). TCF4$^+$ cells found in the corpus callosum at P35 were far fewer than P14, and these cells appeared as clusters (Figure 2-figure supplement 1E). Interestingly, in *Sox10*$^{+/rtTA}$ mice at P35, YFP$^+$ cells were mostly found in regions with TCF4$^+$ cell clusters (Figure 2-figure supplement 1E), where approximately 56% of YFP$^+$ cells were TCF4$^+$ 1 day after virus injection and it reduced to 29% after 1 more day (Figure 2F,G). The half reduction of NFO percentage in YFP$^+$ cells from day 1 to day 2 was consistent with the previous report that NFOs differentiate into MOs in 1 or 2 days (*Xiao et al., 2016*). There was another possibility that the transcriptional activity of *Sox10*-rtTA was low in MOs, and thus took more days to generate detectable YFP levels. We analyzed the densities of TCF4$^+$YFP$^+$ cells and found that they reduced to half from day 1 to day 2 after viral infection in *Sox10*$^{+/rtTA}$ mice at either P14 or P35 (Figure 2H). The results excluded the possibility that the reduction of NFO ratio in YFP$^+$ cells was due to the increase of targeted MOs, and confirmed the maturation of labeled NFOs from day 1 to day 2. A similar transition

196 rate is applicable for targeted NFOs from day 0 to day 1. Therefore, these results
197 corroborate that the majority of cells targeted by *Sox10*-rtTA at the time of AAV-
198 *TRE*-YFP infection were tOPCs and NFOs (Figure 2I).

199 AAV-*TRE*-YFP in *Plp*-tTA mice also labeled some $TCF4^+$ cells, which
200 comprised only 7-12% of YFP^+ cells 1 or 2 days after virus injection at either age
201 (Figure 2E-H). It was noticeable that *Plp*-tTA did not specifically target $TCF4^+$ cell
202 clusters in the corpus callosum at P35 (Figure 2-figure supplement 1F). These results
203 implied that *Plp*-tTA did not specifically target the tOPC or NFO stage but randomly
204 expressed in the OPC-NFO period at a low ratio. Conversely, 90% of the YFP^+ cells
205 were $TCF4^-$ and 92-97% were $CC1^+$ in *Plp*-tTA mice at either P14 or P35, suggesting
206 that *Plp*-tTA steadily targets MOs after early development (Figure 2I).

207

208 **ErbB overactivation causes MO necroptosis and OPC apoptosis**

209 With an understanding of the differentiation stage-specific targeting preferences of
210 $Sox10^{+/rtTA}$ and *Plp*-tTA mice, we investigated the cellular mechanisms that determine
211 the different myelin responses in *Plp*-$ErbB2^{V664E}$ and *Sox10*-$ErbB2^{V664E}$ mice. We
212 found intact post-mitotic OLs ($CC1^+$) decreased in the corpus callosum of *Plp*-
213 $ErbB2^{V664E}$ mice starting from 6 dpd (Figure 3A-C). The $CC1^+$ cells with striking
214 number reduction were MOs because the densities of NFOs ($TCF4^+$) did not show
215 significant change (Figure 3-figure supplement 1B,C). Meanwhile, OPCs
216 ($NG2^+Olig2^+$) pathologically regenerated ($Ki67^+Olig2^+$) in the trunk of corpus
217 callosum, indicating that the pathogenetic factor was released in the myelin-enriched
218 region (Figure 3-figure supplement 1A-E).

MO number reduction occurred earlier than the time when demyelination was obviously observed in the corpus callosum of *Plp*-ErbB2^{V664E} mice, suggesting that oligodendropathy may be the cause of demyelination. We examined the corpus callosum of *Plp*-ErbB2^{V664E} mice by TdT-mediated dUTP nick end labeling (TUNEL) assay, and observed as little apoptotic signaling as that in controls (Figure 3D,E). This result reveals that the degenerating CC1^{+} cells were necrotic rather than apoptotic. Consistently, the OL nuclei associated with the destroyed myelin sheaths in *Plp*-ErbB2^{V664E} mice were regular nuclei without apoptotic chromatin condensation (Figure 1-figure supplement 2A). In support of this theory, MLKL, the protein mediating cell necroptosis (*Cai et al., 2014*) as well as the peripheral myelin breakdown after nerve injury (*Ying et al., 2018*), demonstrated an increased expression in the callosal CC1^{+} cells in *Plp*-ErbB2^{V664E} mice from 6 dpd (Figure 3F-H). Necroptosis is a programmed form of necrosis. RIP3 is the kinase at the upstream of MLKL in this programmed death signaling pathway (*Ofengeim et al., 2015; Sun et al., 2012*). Notably, the expression of RIP3 was also elevated in the callosal CC1^{+} cells in *Plp*-ErbB2^{V664E} mice from 6 dpd as revealed by both immunostaining and western blotting (Figure 3F-H). Based on the timeline, MO necroptosis was the primary defect induced in *Plp*-ErbB2^{V664E} mice, followed by myelin breakdown, OPC regeneration, axonal degeneration, and other pathological events as reported in multiple sclerosis (*Bradl and Lassmann, 2010; Ofengeim et al., 2015*).

In contrast, for *Sox10*-ErbB2^{V664E} mice, a dramatic increase in cell apoptosis (TUNEL^{+}) in the corpus callosum was observed (Figure 3E,I,J). These apoptotic nuclei were localized in NG2^{+} cells (Figure 3K), indicating apoptosis of OPCs. On the other hand, no increase of MLKL or RIP3 was detected (Figure 3G,H,L), indicating there was no necroptosis. Notably, both the NG2^{+} cells with and without TUNEL^{+}

nuclei were hypertrophic in *Sox10*-ErbB2^{V664E} mice (Figure 3K). This phenomenon was not revealed for NG2^{+} cells in *Plp*-ErbB2^{V664E} mice (Figure 3-figure supplement 1B).

ErbB inhibition in OPC-NFOs, but not in MOs, induces hypomyelination

Next, to investigate whether ErbB receptors are functionally required for OLs, we examined the effects of inhibiting ErbB activities in different OL stages on CNS myelin. To this end, we first generated *Sox10*$^{+/rtTA}$;*TRE*-dnEGFR (*Sox10*-dnEGFR) mice (Figure 4A and Figure 4-figure supplement 1A,B). In line with the inhibitory effect of dnEGFR on endogenous ErbB activities (*Chen et al., 2017*), phosphorylation of ErbB3 and ErbB4 was reduced in white matter from *Sox10*-dnEGFR mice at P35 (Figure 4B,C). The phosphorylation of EGFR was not altered in *Sox10*-dnEGFR mice at P35 (Figure 4B,C), consistent with the finding in *Sox10*-ErbB2^{V664E} mice (Figure 1N,O). Myelin thickness and ultrastructures in the white matter of *Sox10*-dnEGFR and littermate control mice at P35 with 14 dwd did not show significant differences (Figure 4-figure supplement 1C). Therefore, we raised these mice to adulthood with continuous Dox feeding. Phosphorylation of EGFR, instead of ErbB3 or ErbB4, was apparently reduced in the white matter of *Sox10*-dnEGFR mice at P65 (Figure 4B,C). This change of ErbB receptors targeted by dnEGFR in *Sox10*-dnEGFR mice implied a switch of functional NRG-ErbB signaling to EGF-ErbB signaling in *Sox10*-rtTA-targeted cells from adolescence to adulthood.

For *Sox10*-dnEGFR mice at P65 with 44 dwd, myelin stained by LFB exhibited reduced intensity in the trunk of the corpus callosum (Figure 4D). Moreover, axons in the corpus callosum and optic nerve of *Sox10*-dnEGFR mice at P65 were

hypomyelinated in comparison with that of littermate controls (Figure 4E). Consistently, MBP was reduced in the white matter of *Sox10*-dnEGFR mice at P65 (Figure 4B,C). Therefore, ErbB inhibition in OPC-NFOs starting from P21 results in hypomyelination in adulthood.

On the other hand, we crossed *Plp*-tTA and *TRE*-dnEGFR to generate *Plp*-tTA;*TRE*-dnEGFR (*Plp*-dnEGFR) mice (Figure 4F and Figure 4-figure supplement 1D,E). Western blotting revealed significant suppression on the phosphorylation of EGFR, as well as a mild suppression on that of ErbB3 and ErbB4 (Figure 4G,H), consistent with their overactivation in *Plp*-ErbB2^{V664E} mice (Figure 1C,D). No CNS myelin differences were observed in *Plp*-dnEGFR and littermate control mice at P35 with 14 dpd (Figure 4-figure supplement 1F).

We extended our investigation to P65 when dnEGFR still functionally suppressed ErbB receptor activities in the white matter of *Plp*-dnEGFR mice (Figure 4G,H). Even in the adult mice, when dnEGFR had been expressed in MOs for 44 days, the brains of *Plp*-dnEGFR and littermate mice exhibited no difference in LFB-stained myelin (Figure 4I), MBP protein levels (Figure 4G,H), or myelin ultrastructures (Figure 4J). These results suggest that the dual blockade of endogenous NRG-ErbB and EGF-ErbB signaling in MOs does not affect CNS myelin integrity, and that ErbB activities are not required for the maintenance of CNS myelin after maturation.

ErbB activation blocks OPC proliferation and survival, whereas promotes NFO differentiation and myelination

It is intriguing to note that both ErbB inhibition and overactivation in OPC-NFOs result in hypomyelination in the CNS. This implies that ErbB signaling can regulate

CNS myelin development by different mechanisms. To investigate the mechanisms, we first compared the states of OL lineage cells in *Sox10*-ErbB2^{V664E} and *Sox10*-dnEGFR mice. In line with the finding that OPCs underwent apoptosis, the numbers of Olig2$^+$, NG2$^+$, and CC1$^+$ cells significantly decreased in the corpus callosum of *Sox10*-ErbB2^{V664E} mice (Figure 5A and Figure 5-figure supplement 1A), while there was no OPC or OL differences between *Sox10*$^{+/rtTA}$ and *TRE*-ErbB2^{V664E} littermates at P30 with 9 dwd (Figure 5-figure supplement 1A). Further, we found proliferating OPCs (Ki67$^+$Olig2$^+$) significantly decreased in the corpus callosum of *Sox10*-ErbB2^{V664E} mice (Figure 5D,G). In contrast, the densities of proliferating OPCs (Ki67$^+$Olig2$^+$) and Olig2$^+$ cells increased in *Sox10*-dnEGFR mice at P65 (Figure 5B,E,G and Figure 5-figure supplement 1B), despite the fact that these increases were not observed in *Sox10*-dnEGFR mice at P35 (Figure 5-figure supplement 2A-C). No pathological signs were observed and the increased Olig2$^+$ cells comprised of both NG2$^+$ and CC1$^+$ cells (Figure 5B and Figure 5-figure supplement 1B). It could not be determined whether apoptosis decreased in *Sox10*-dnEGFR white matter, as the apoptotic cells (TUNEL$^+$) were minimal in white matter of both *Sox10*-dnEGFR and control mice (Figure 5H). The consistent results from gain-of-function (*Sox10*-ErbB2^{V664E}) and loss-of-function (*Sox10*-dnEGFR) studies support a negative regulation of OPC proliferation and survival by ErbB signaling.

Neither differences in Olig2$^+$, CC1$^+$, NG2$^+$, or Ki67$^+$Olig2$^+$ cell densities (Figure 5C,F,G; Figure 5-figure supplement 1C; Figure 5-figure supplement 2D-F), nor in TUNEL$^+$ cells (Figure 5I), were observed in white matter of *Plp*-dnEGFR mice and littermate controls at P35 or P65. Different cellular and histological phenotypes in *Sox10*-dnEGFR and *Plp*-dnEGFR mice consolidated again the different targeting specificities of *Sox10*$^{+/rtTA}$ and *Plp*-tTA. Moreover, the conflicting observations that

317 the numbers of post-mitotic OLs ($CC1^+$) increased but myelin thickness reduced in
318 the brain of *Sox10*-dnEGFR mice (Figure 4E and Figure 5B), suggested that ErbB
319 inhibition in OPC-NFOs had significantly impaired the myelinating capacity of OLs.

320 Given that *Sox10*-dnEGFR and *Sox10*-ErbB2^{V664E} mice both exhibited
321 hypomyelination, they should share a molecular or cellular deficit in myelination. We
322 performed RNA-seq analyses of subcortical white matter tissues and identified 68
323 genes which exhibited similar expression tendencies in *Sox10*-ErbB2^{V664E} and *Sox10*-
324 dnEGFR mice (Figure 6A). This group of genes have potential to regulate CNS
325 myelination. Notably, in addition to *Gsn* and *Itgb4* that have been identified as
326 characteristic genes for myelinating OLs (*Zhang et al., 2014*), *Enpp6*, *Itpr2*, and
327 *Slc12a2* as characteristic genes for NFOs also exhibited significantly reduced
328 expression in both mouse lines, supporting the notion that NFO deficiency contributes
329 to hypomyelination. We examined the distribution of *Enpp6*-expressing cells by *in*
330 *situ* hybridization (*Xiao et al., 2016*), and found that *Enpp6*$^+$ cell numbers were indeed
331 reduced in the corpus callosum of *Sox10*-dnEGFR mice at P35, although the reduction
332 became indistinguishable for mice at P65 (Figure 6C,E). We further examined NFOs
333 by immunostaining for TCF4, and found TCF4$^+$ cell numbers were also reduced in the
334 corpus callosum of *Sox10*-dnEGFR mice at P35, although the reduction became
335 indistinguishable for mice at P65 (Figure 6G,I). Therefore, NFO differentiation was
336 impaired shortly after ErbB inhibition, although it took 44 days to result in obvious
337 hypomyelination in *Sox10*-dnEGFR mice. TCF4$^+$ and *Enpp6*$^+$ cell numbers were also
338 reduced in *Sox10*-ErbB2^{V664E} mice (Figure 6B,F,E,I), which were due to the shortage
339 of OPCs for differentiation.

340 Interestingly, we also observed lowered TCF4$^+$ and *Enpp6*$^+$ cell numbers in *Plp*-
341 dnEGFR mice at P35 (Figure 6D,E,H,I). *Plp*-tTA targeted a fraction of NFOs (Figure

342 2E-I). The different myelination states and similar NFO number reduction in *Sox10*-
343 dnEGFR and *Plp*-dnEGFR mice suggest that, besides regulating myelinating
344 capability of NFOs, ErbB signaling separately regulates another aspect of NFO
345 differentiation, *i.e.*, the transition time from NFO to MO stage. Indeed, in contrast to
346 that in *Sox10*-dnEGFR and *Plp*-dnEGFR mice, the ratio of $TCF4^+$ to $CC1^+$ cell
347 densities increased in *Sox10*-$ErbB2^{V664E}$ mice (Figure 6J), which may suggest a
348 prolonged transition to the MO stage for NFOs with ErbB activation.

349

350 **ErbB inhibition in MOs disrupts cognitive function in the absence of myelin**
351 **alteration**

352 OLs also offer essential trophic support to neurons in addition to forming myelin
353 (*Nave and Werner, 2014*). We compared the behavioral performance of *Sox10*-
354 dnEGFR mice, with hypomyelination in most brain regions, and *Plp*-dnEGFR mice,
355 with normal myelin, to investigate whether disrupting ErbB signaling in MOs induces
356 deficits other than dysmyelination. *Sox10*-dnEGFR mice performed worse than
357 control mice in the rotarod test (Figure 7A), and were slightly hypoactive in the open
358 field test (Figure 7B). Nevertheless, they performed normally in the central/peripheral
359 zone analysis for assessment of anxiety, stereotyped behavior analysis and social
360 interaction analysis for potential autistic-like phenotype, prepulse inhibition analysis
361 for sensory gating, as well as forced swim and tail suspension tests for depression
362 (Figure 7-figure supplement 1A-E). Interestingly, *Plp*-dnEGFR mice performed
363 normally, similar to the controls in most tests, except exhibiting a subtle hyperactivity
364 in the open field test (Figure 7C,D and Figure 7-figure supplement 1F-J). The

365 different results from the two mouse lines implied that the impaired motor
366 coordination could be attributed to the hypomyelination in the CNS.

367 We further tested these mice in the eight-arm radial water maze, a paradigm
368 analyzing working memory capacity. It is known that myelin integrity is fundamental
369 to cognitive performance of patients (*Kujala et al., 1997*). Moreover, although
370 ErbB3/ErbB4 double knock-out does not induce myelin alteration in the CNS during
371 early postnatal development (*Brinkmann et al., 2008*), a study of specifically
372 depleting ErbB3 in mice from P19 has associated CNS hypomyelination with working
373 memory deficits in adult mice (*Makinodan et al., 2012*). However, not only *Sox10*-
374 dnEGFR mice, which had CNS hypomyelination, but also *Plp*-dnEGFR mice, which
375 did not have myelin alteration, had significantly more working memory errors than
376 control mice (Figure 7E,F and Figure 7-Video 1). Note that they had normal eyesight
377 as performed in the visible platform test, as well as similar reference memory errors
378 that indicated unaltered spatial recognition and memory (Figure 7E,F). This
379 phenotype in *Plp*-dnEGFR mice reveals that working memory deficiency can be
380 caused directly by ErbB inhibition in MOs through a myelination-independent
381 mechanism.

382

383 **ErbB inhibition in MOs suppresses axonal conduction under energy stress**

384 To determine what kind of function was impaired in white matter tracts of *Plp*-
385 dnEGFR mice, we acutely isolated the optic nerves from adult mice (P90-P110) and
386 recorded electrical stimulus-evoked compound action potentials (CAPs). The areas
387 under CAPs, which are proportional to the total number of excited axons, indicate the
388 nerve conduction. We found comparable areas under CAPs in *Plp*-dnEGFR optic

389 nerves and control nerves responding to stimuli of the same intensity (Figure 7G). The
390 maximal CAPs, which represent that all axons in the nerves are excited, were similar
391 in *Plp*-dnEGFR optic nerves and control nerves (Figure 7G). In contrast, they were
392 reduced in *Sox10*-dnEGFR optic nerves as compared with littermate controls (Figure
393 7H). These results reflected that the basic axonal conduction was not affected in *Plp*-
394 dnEGFR white matter tracts, whereas it was impaired in *Sox10*-dnEGFR white matter
395 tracts that exhibited hypomyelination.

396 In addition to myelin, macroglial metabolites are important for axonal conduction
397 maintenance under conditions of energy deprivation (*Funfschilling et al., 2012; Saab*
398 *et al., 2016; Trevisiol et al., 2017*). We challenged the optic nerves by incubating
399 them in the oxygen-glucose deprivation (OGD) condition for 60 min. CAPs fell
400 gradually in control optic nerves, and finally fell to 30% of the initial levels (Figure
401 7I,J). However, for *Plp*-dnEGFR optic nerves in the OGD condition, CAP failure was
402 slightly accelerated and aggravated (Figure 7I). Contrarily, for *Sox10*-dnEGFR optic
403 nerves under the same condition, CAP failure was decelerated and attenuated (Figure
404 7J). When the glucose and oxygen levels in the bathing medium were restored, CAPs
405 in control optic nerves and *Plp*-dnEGFR optic nerves recovered to 60% of the initial
406 levels (Figure 7I,J). However, in *Sox10*-dnEGFR optic nerves, CAPs recovered to 80%
407 of the initial levels (Figure 7J).

408 It is notable that continuous electrical stimulation caused a baseline CAP decline
409 in *Plp*-dnEGFR optic nerves, whereas a baseline CAP enhancement in *Sox10*-
410 dnEGFR optic nerves, before the OGD (Figure 7I,J). Therefore, we further examined
411 the axonal conduction under a physiological condition with increasing energy
412 demands generated by neuronal activities (*Saab et al., 2016; Trevisiol et al., 2017*).
413 By stimulating the control optic nerves with several trains of short bursts with

414 frequency increased from 1 to 100 Hz, we confirmed that the low frequency
415 stimulation (5-25Hz) has only minor influence on the CAPs, whereas the high
416 frequency stimulation (50-100Hz) exhausts axonal energy and results in CAP decline
417 (Figure 7K,L). For *Sox10*-dnEGFR optic nerves, intriguingly, the 5-25Hz electrical
418 stimuli amplified CAPs and the 50-100Hz stimuli induced smaller CAP decay than
419 that in control nerves (Figure 7L). In contrast, in *Plp*-dnEGFR optic nerves, either
420 group of stimuli significantly aggravated the CAP decay (Figure 7K).

421 These results showed that *Sox10*-dnEGFR white matter tracts exhibited resistance
422 to energy stress induced by both pathological (OGD) and physiological (neuronal
423 activities) conditions. This may be ascribed to increased OL numbers, as that OLs are
424 an essential venue for glycolysis and energy substrate production in support of axonal
425 conduction (*Funfschilling et al., 2012*). In contrast, *Plp*-dnEGFR white matter was
426 deficient in the maintenance of axonal conduction, especially under physiological
427 energy stress. It is notable that MO numbers were not altered in *Plp*-dnEGFR mice
428 that have ErbB inhibition in MOs, whereas ErbB receptors were not inhibited in MOs
429 of *Sox10*-dnEGFR mice that have increased MOs (Figure 5B,C). Therefore, the
430 opposite results of *Sox10*-dnEGFR and *Plp*-dnEGFR optic nerves in the energy
431 challenging studies reveal that ErbB inhibition in MOs impairs the glia-axon energy
432 coupling efficiency within electrically active neural circuits, which can compromise
433 the cognitive function in *Plp*-dnEGFR mice in the absence of myelin alteration
434 (Figure 7F).

435

436

437 **Discussion**

Our results demonstrate that both ErbB3/ErbB4 receptors binding to the NRG family ligands and EGFR binding to the EGF family ligands are functional in adolescent and adult OLs. With the discovery of two valuable *in vivo* research mouse tools that differentially target OLs at MO and OPC-NFO stages, we reveal that NRG-ErbB and EGF-ErbB signaling cooperate in OPCs, NFOs, and MOs to simultaneously regulate myelination and axonal energy supporting functions. Aberrant ErbB activation or inhibition causes white matter abnormalities with distinct pathological characteristics and biological markers (Figure 7M).

ErbB overactivation is pathogenetic in MOs through inducing myelin overproduction and MO necroptosis, which results in demyelination followed by pathological changes including axon degeneration, OPC regeneration, astrogliosis and microgliosis. Notably, ErbB overactivation in OPCs induces apoptosis, without stimulating inflammatory pathological responses in the brain (Figures 1 and 3). Caspase-8 activation has been reported to be the key event to determine apoptotic fate of cells (*Oberst et al., 2011*), and defective activation of caspase-8 is critical for RIP1/RIP3/MLKL signaling to induce OL necroptosis in multiple sclerosis (*Ofengeim et al., 2015*). A cell-type specific RNA-sequencing transcriptome analysis suggests that caspase-8 is minimally expressed in post-mitotic OLs but is detectable in OPCs (*Zhang et al., 2014*), which may determine MO necroptosis but OPC apoptosis under continuous ErbB activation. Interestingly, studies on genetically modified mice that overexpressing hEGFR in OL lineage cells, or overexpressing NRG1 Type I or Type III in neurons, did not report myelin pathogenesis (*Aguirre et al., 2007; Brinkmann et al., 2008*). Nevertheless, mice with overactivation of the ErbB downstream signaling in OL lineage cells exhibit myelin and axonal pathology (*Harrington et al., 2010; Ishii et al., 2016*). *Olig2*-cre;Pten$^{flox/flox}$ mice that overactivate PI3K/Akt signaling in

OL lineage cells have loosened myelin lamellae in the spinal cord at 14 weeks and axonal degeneration in the cervical spinal cord fasciculus gracilis at 62 weeks (*Harrington et al., 2010*). *Plp*-CreER;Mek/Mek mice, which overexpress a constitutively activated MEK, a MAPK kinase, in OL lineage cells with tamoxifen induction, show demyelination in the spinal cord 3 months after MAPK (Erk) overactivation is induced (*Ishii et al., 2016*). Devastating effects of ErbB2^{V664E} in OLs may be due to its potent promotion of endogenous ErbB activation and multiple downstream signaling. Nevertheless, observations in the present study and in *Olig2*-cre;Pten$^{flox/flox}$ and *Plp*-CreER;Mek/Mek mice corroborate the concept that constitutively activating ErbB signaling in OL lineage cells is pathogenetic, even though it may take a long time for moderate activation to result in pathological symptoms.

The profound demyelination or hypomyelination in *Plp*-ErbB2^{V664E} and *Sox10*-ErbB2^{V664E} mice should have disrupted many brain functions, although we could not evaluate these functions in the two strains by behavioral tests due to their severe motor dysfunction (Figure 1B,M). Intriguingly, a battery of behavioral tests for *Sox10*-dnEGFR and *Plp*-dnEGFR mice only revealed working memory deficits for both of them, except for the impaired motor coordination in *Sox10*-dnEGFR mice that have moderate hypomyelination (Figure 7A-F and Figure 7-figure supplement 1A-J). The further analyses emphasize that, although endogenous ErbB activation is required for both NFOs and MOs, it is used for the control of myelination and glia-axon energy coupling, respectively. Thus, ErbB inhibition in OLs impairs cognitive functions *via* myelination-dependent and -independent mechanisms. *Plp*-dnEGFR mice are a good model to affirm the myelination-independent contributions of OLs to higher brain function. As exhibited in *Plp*-dnEGFR mice, dual inhibition of NRG-ErbB and EGF-

ErbB signaling in MOs does not affect myelin or OL numbers in the adolescent and adult brains. However, endogenous ErbB activities in MOs are indispensable for the maintenance of axonal conduction under physiological energy stress (Figure 7I,K), which are important for neuronal circuit efficiency as well as cognitive performance (Figure 7F). It is interesting that axonal conduction under energy stress was enhanced in *Sox10*-dnEGFR white matter tracts (Figure 7J,L), although it remains unclear whether the improved energy supplementation alleviates or aggravates the cognitive deficits in *Sox10*-dnEGFR mice (Figure 7E). Multiple questions remain unanswered, such as ErbB signaling regulates glucose metabolism in MOs or the transportation of energy metabolites from MOs to axons. ErbB dysregulation disrupts glutamatergic synaptic transmission in neurons (*Luo et al., 2014; Ting et al., 2011; Woo et al., 2007*). Glutamatergic synaptic transmission onto OLs was recently discovered to be essential for their energy substrate supply to axons (*Saab et al., 2016*), as well as for OL development (*Kougioumtzidou et al., 2017*). Therefore, it would be worth pursuing whether ErbB signaling regulates OL development or the trophic support from MOs to neurons by modulating glutamatergic synaptic transmission on OLs.

The roles of ErbB signaling in CNS myelination have long been debated because of the contradictory findings reported by different research groups. For example, ErbB3 has been reported to be dispensable for OL development (*Schmucker et al., 2003*), and ErbB3/ErbB4 double knockout does not result in CNS myelin alteration (*Brinkmann et al., 2008*). However, there are other reports that indicate inducing ErbB3 depletion by *Plp*-CreER in OL lineage cells from P19, not P36, results in adult hypomyelination (*Makinodan et al., 2012*). It is notable that ErbB3 has peaked expression during P15-P30 (Figure 1-figure supplement 1), and ErbB receptor manipulation in OPC-NFOs alters ErbB3/4 activities in white matter at P30-35 but not

513 at P65 (Figure 1N and Figure 4B). Note that *Plp*-CreER is a mouse tool that can target
514 OPCs and their progeny (*Guo et al., 2009*). Therefore, the hypomyelination in *Plp*-
515 CreER;ErbB3$^{flox/flox}$ mice is in line with our findings in *Sox10*-dnEGFR mice and
516 reflects the positive role of ErbB signaling in NFO myelination during late postnatal
517 development. EGFR is expressed stably in white matter during P20-P40 (Figure 1-
518 figure supplement 1). The phosphorylation of EGFR is altered in white matter in all
519 four mouse strains, which have ErbB receptor manipulation either in MOs or in OPC-
520 NFOs (Figure 1C,N and Figure 4B,G). This suggests the general involvement of
521 EGFR in OL function and development. The role of EGFR in CNS myelin
522 development is supported by the report that transgenic mice with overexpression of
523 hEGFR in all OL lineage cells (*CNP*-hEGFR) have enhanced myelin maturation, and
524 hypomorphic EGFR mice (wa2) have delayed myelin maturation (*Aguirre et al.,*
525 *2007*). *CNP*-hEGFR mice exhibit enhanced oligodendrogenesis in the subventricular
526 zone, reflecting the function of EGFR in promoting neural progenitors to differentiate
527 into OPCs during the early development (*Aguirre et al., 2007*). This is different from
528 the pathological OPC regeneration revealed in the corpus callosum of *Plp*-ErbB2^{V664E}
529 mice. It is notable that *CNP*-hEGFR increases the numbers of myelinated axons but
530 not myelin thickness (*Aguirre et al., 2007*), which is different from the
531 hypermyelination phenotype revealed in the CNS of NRG1-overexpressing mice
532 (*Brinkmann et al., 2008*), suggesting that EGFR unlikely participates in myelin
533 overproduction in MOs. It will be interesting to know whether the active EGFR, as
534 revealed in *Plp*-dnEGFR mice (Figure 4G), is required for the trophic supportive
535 function of MOs.

536 The negative regulation of ErbB activation on OPC proliferation and survival is
537 unexpected because many *in vitro* studies have suggested otherwise. However, there

538 is an interesting observation in transgenic mice *CNP*-dnErbB4, which are designed to
539 overexpress a dominant negative ErbB4 mutant that specifically blocks the activities
540 of ErbB3 and ErbB4 in all OL lineage cells. In this strain, post-mitotic OL numbers
541 increase 40% in the corpus callosum although axons are hypomyelinated (*Roy et al.,*
542 *2007*). Moreover, *Olig2*-cre;Pten$^{flox/flox}$ mice, which have activation of the PI3K/Akt
543 pathway in all OL lineage cells, exhibit hypermyelination but decreased OL densities
544 in the developing corpus callosum (*Harrington et al., 2010*). These previously
545 enigmagic observations are now well-explained by our findings that ErbB signaling
546 plays different roles in OPCs and NFOs.

547 The white matter abnormalities observed in our mouse models are reminiscent of
548 diverse myelin-related clinical and pathological characteristics in schizophrenic brains,
549 including reduced white matter volume, decreased OL densities, reduced myelin gene
550 products, apoptotic OLs, and damaged myelin (*Douaud et al., 2007; Fields, 2008;*
551 *Hoistad et al., 2009; Uranova et al., 2011; Uranova et al., 2007*). Elevated ErbB
552 activation has been repeatedly implicated in schizophrenia, and the increase could be
553 caused by genetic factors (*Harrison and Law, 2006; Law et al., 2012*). To our
554 knowledge, we are the first to reveal that ErbB overactivation can primarily induce
555 oligodendropathy and myelin pathogenesis in white matter, providing a possible
556 predisposition of a genetic variability in ErbB receptors or ligands to the white matter
557 lesion. Notably, SNP8NRG243177 with T-allele, which increases NRG1 Type IV
558 production (*Law et al., 2006*), is associated with the reduced white matter integrity
559 (*McIntosh et al., 2008*) as well as increased psychotic symptoms (*Hall et al., 2006*) in
560 schizophrenic patients.

561 Further, ErbB receptors and their ligands have been reported to reduce expression
562 or lose function in some schizophrenic patients (*Harrison and Law, 2006; Mei and*

563 *Nave, 2014*). Specific working memory deficits in *Sox10*-dnEGFR and *Plp*-dnEGFR
564 mice firmly support that oligodendropathy can be a primary cause for the cognitive
565 symptoms of schizophrenia. Moreover, myelin is very sensitive to environmental
566 insults. Modest disruption of ErbB signaling by genetic mutation or SNPs is able to
567 render myelin vulnerable to such insults, aggravating focal loss of connections under
568 conditions of stress, ischemia, sleeplessness, trauma, etc. Therefore, OL dysfunction
569 in patients, which is difficult to measure with current techniques, may eventually
570 evolve into a detectable structural alteration in white matter that could contribute to
571 another type of brain dysfunction. Collectively, our study provides novel insights into
572 the pathophysiology of diseases initiated or aggravated within white matter.

573

574

575 # Materials and methods

576 ## Animals

577 *Plp*-tTA transgenic mice (*Inamura et al., 2012*) were from the RIKEN BioResource
578 Center (Stock No. RBRC05446). *Sox10*$^{+/rtTA}$ mice were from Dr. Michael Wegner
579 (University Erlangen-Nurnberg, Germany). Transgenic mice *TRE*-ErbB2^{V664E} (Stock
580 No. 010577) and *TRE*-dnEGFR (Stock No. 010575) were from the Jackson
581 Laboratory (*Chen et al., 2017*). Among ErbB1-4 receptors, ErbB2 that does not bind
582 to any known ligand is the preferred partner to other ligand-bound ErbB members.
583 ErbB2^{V664E} contains an amino acid mutation (Vla_{664}/Glu_{664}) within the transmembrane
584 domain facilitating its dimerization with other ErbB receptors and potentiating their
585 downstream signaling (*Chen et al., 2017*). DnEGFR, a dominant negative mutant of
586 EGFR, is a truncated form of EGFR, losing the intracellular kinase domain but

retaining the ability to form dimers with other ligand-bound ErbB members. When overexpressed, dnEGFR efficiently blocks the activation of any endogenous ErbB receptors under either NRG or EGF stimulation (*Chen et al., 2017*). Unless indicated, mice were housed under SPF conditions before experiments, in a room with a 12-hr light/dark cycle with access to food and water *ad libitum*. For biochemical and histological experiments, *Plp*-tTA;*TRE*-dnEGFR (*Plp*-dnEGFR), *Plp*-tTA;*TRE*-ErbB2^{V664E} (*Plp*-ErbB2^{V664E}), *Sox10*$^{+/rtTA}$;*TRE*-dnEGFR (*Sox10*-dnEGFR), or *Sox10*$^{+/rtTA}$;*TRE*-ErbB2^{V664E} (*Sox10*-ErbB2^{V664E}) mice with either sex and their littermate control mice with matched sex were used. For indicated behavioral tests, only male mice were used, while both male and female mice were used for the other behavioral tests because the results were not affected by sex difference. Animal experiments were approved by the Institutional Animal Care and Use Committee of the Hangzhou Normal University. For genotyping, the following primers were used: for *Plp*-tTA (630bp), PLPU-604 5'-TTT CCC ATG GTC TCC CTT GAG CTT, mtTA24L 5'-CGG AGT TGA TCA CCT TGG ACT TGT; for Sox10$^{+/rtTA}$ (618bp), sox10-rtTA1 5'-CTA GGC TGT CAG AGC AGA CGA, sox10-rtTA2 5'-CTC CAC CTC TGA TAG GT CTT G; for *TRE*-dnEGFR (318bp), 9013 5'-TGC CTT GGC AGA CTT TCT TT, 7554 5'-ATC CAC GCT GTT TTG ACC TC; for *TRE*-ErbB2^{V664E} (625bp), 9707 5'-AGC AGA GCT CGT TTA GTG, 9708 5'-GGA GGC GGC GAC ATT GTC.

Tet-Off or Tet-On treatment of mice

Mice with Tet-system contain genes of tetracycline-controlled transcriptional activator (tTA) or reverse tetracycline-controlled transcriptional activator (rtTA) driven by cell-

specific promoters. When fed with Dox, these mice are able to switch on or off expression of a gene under the control of *tetracycline-responsive element* (*TRE*), specifically in rtTA- or tTA-expressing cells, which are called 'Tet-on' or 'Tet-off', respectively. The offspring of *Sox10*$^{+/rtTA}$ during the indicated periods were fed with Dox (2 mg/mL × 10 mL/day from P21 to P35, and 1 mg/mL × 10 mL/day from P35 to indicated test day) in drinking water to induce the expression of ErbB2^{V664E} or dnEGFR in *Sox10*-ErbB2^{V664E} and *Sox10*-dnEGFR mice, respectively (Tet-On). For the offspring of *Plp*-tTA, Dox was given (Tet-off) from the embryonic day (through pregnant mothers) to their weaning day at P21 to inhibit the expression of ErbB2^{V664E} or dnEGFR during this period in *Plp*-ErbB2^{V664E} or *Plp*-dnEGFR mice (0.5 mg/mL × 10 mL/day of Dox before P21). Water bottles were wrapped with foil to protect Dox from light. All used littermate control mice were treated the same.

Stereotactic injection of AAV viruses

pAAV-*TRE*-EYFP plasmids (Addgene) were packaged as AAV2/9 viruses, and produced with titers of 2.0E+13 particles per mL by OBio (Shanghai, China). Mice were anesthetized by 1% pentobarbital (50 mg/kg, i.p.) and mounted at stereotaxic apparatus (RWD68025). AAV-*TRE*-EYFP (2 μL) was injected into the corpus callosum (from bregma in mm, M-L: ±1.2, A-P: +0.5, D-V: -2.2) under the control of micropump (KDS310) at a speed of 0.05 μL/min. Injecting needles (Hamilton NDL ga33/30 mm/pst4) were withdrawn 10 min after injection. Infected brains were isolated 1 or 2 days later and brain slices were immunostained with anti-GFP antibody to enhance the visualization of the reporter protein.

635 **Electron Microscopy**

636 Mice were anesthetized and transcardially perfused with 4% sucrose, 4%
637 paraformaldehyde (PFA) and 2% glutaraldehyde in 0.1 M phosphate buffer (PB, pH
638 7.4). The brains, optic nerves, or sciatic nerves were isolated carefully. The corpora
639 callosa and prefrontal cortices were further dissected carefully under stereoscope.
640 Tissues were post-fixed overnight at 4°C in 1% glutaraldehyde in 0.1 M PB. Samples
641 were washed by 0.1 M PB 24 hr later, and osmicated with 2% osmium tetroxide 30-
642 60 min at 4°C, washed by 0.1 M PB and by deionized H_2O at 4°C, and dehydrated in
643 graded (50-100%) ethanol. Samples were incubated with propylene oxide and
644 embedded with embedding resins. Ultrathin sections were stained with 2% uranyl
645 acetate at 4°C for 30 min, and then photographed with Tecnai 10 (FEI). EM images
646 were analyzed by Image J (NIH). To eliminate the bias on circularity, *g*-ratio of each
647 axon was calculated by the perimeter of axons (inner) divided by the perimeter of
648 corresponding fibers (outer). Axonal diameters were normalized by perimeters
649 through equation: diameter = perimeter/π. This procedure allows for inclusion of
650 irregularly shaped axons and fibers and helps to eliminate biased measurement of
651 diameters based on circularity. For quantitative analysis, cross sections of each neural
652 tissue were divided into 5 areas, and more than two images, randomly selected from
653 each area, were examined.

654

655 **Immunofluorescence staining**

656 Deeply anesthetized mice were transcardially perfused with 0.01 M PBS and then 4%
657 PFA in 0.01 M PBS. Mouse brains were isolated and post-fixed in 4% PFA in 0.01 M
658 PBS overnight at 4 °C, and then transferred into 20% and subsequently 30% sucrose

in PBS overnight at 4 °C. Brains were then embedded in OCT (Thermo Fisher scientific) and sectioned into 20 μm on a cryostat sectioning machine (Thermo Fisher scientific, Microm HM525). Brain slices were incubated with blocking buffer (10% fetal bovine serum and 0.2% Triton-X-100 in 0.01 M PBS) for 1 hr at room temperature, and then incubated at 4 °C overnight with primary antibodies diluted in blocking buffer. The primary antibodies used were: GFP (1:500, Abcam, ab13970), CC1 (1:500, Abcam, ab16794), NG2 (1:200, Abcam, ab50009), Ki67 (1:400, Cell Signaling Technology, 9129), GFAP (1:2000, Millipore, MAB360), Iba1 (1:1000, Millipore, MABN92), TCF4 (1:500, Millipore, 05-511), Olig2 (1:500, Millipore, AB9610), TUJ1 (1:500, Sigma, T5076), RIP3 (1:500, QED, 2283), MLKL (1:500, Abgent, AP14272B). After washing three times with 0.1% Triton-X-100 in 0.01 M PBS, samples were incubated at room temperature for 1 hr with Alexa-488 or -594 secondary antibody, and then washed and mounted on adhesion microscope slides (CITOTEST) with fluorescent mounting medium. Nuclear labeling was completed by incubating slices with DAPI (0.1 μg/mL, Roche) at room temperature for 5 min after incubation with secondary antibodies. Except for the antibody against NG2, antigen retrieval in 0.01 M sodium citrate buffer (pH 6.0) at 80-90 °C for 10 min was necessary before primary antibody incubation for brain slices to achieve definitive signals. Images were taken by a Zeiss LSM710 confocal microscope or a Nikon Eclipse 90i microscope. For cell counting based on immunostaining results, soma-shaped immunoreactive signals associated with a nucleus was counted as a cell. The immunostaining intensity was measured by Image J with background subtraction.

Luxol fast blue (LFB) staining

After sufficient washing with 0.01 M PBS, PFA-fixed brain slices were transferred into a mixture of trichloromethane and ethanol (volume ratio 1:1) for 10 min and then 95% ethanol for 10 min. They were next incubated in 0.2% Luxol fast blue staining solution (0.2 g Solvent blue 38, 0.5 mL acetic acid, 95% ethanol to 100 mL) at 60 °C overnight. In the next day, tissues were incubated for 5 min each in turn in 95% ethanol, 70% ethanol and ddH_2O for rehydration, followed by incubation alternatively in 0.05% Li_2CO_3, 70% ethanol and ddH_2O for differentiation until the contrast between the gray matter and white matter became obvious. After that, tissues were incubated for 10 min each in 95% and 100% ethanol to dehydrate, and then 5 min in dimethylbenzene to clear, before quickly mounting with neutral balsam mounting medium (CWBIO). All steps were operated in a ventilation cabinet. The LFB intensity in the corpus callosum was measured by Image J with background subtraction, and normalized to that of controls.

TUNEL assay

Apoptotic cells were examined with terminal deoxynucleotidyl transferase (TdT)-mediated deoxyuridine triphosphate (dUTP) nick-end labeling (TUNEL) assay according to the manufacturer's instructions (Vazyme; Yeasen). In brief, PFA-fixed brain slices were digested for 10 min by proteinase K (20 μg/mL) at room temperature. After washing twice with PBS, brain slices were incubated with Equilibration Buffer for 30 min at room temperature, and subsequently with Alexa Fluor 488-12-dUTP Labeling Mix for 60 min at 37°C. After washing with PBS three times, brain slices were stained with DAPI before being mounted under coverslips. For co-labeling of

706 apoptotic nuclei in slices with immunofluorescence staining, TUNEL assay was
707 performed after washing of the secondary antibody.

708

709 **Western blotting**

710 Subcortical white matter tissues were isolated and homogenized. Homogenates in
711 lysis buffer (10 mM Tris-Cl, pH 7.4, 1% NP-40, 0.5% Triton-X 100, 0.2% sodium
712 deoxycholate, 150 mM NaCl, 20% glycerol, protease inhibitor cocktail) at a ratio of 2
713 mL per 100 mg tissue were lysed overnight in 4°C. Lysates were centrifuged at
714 12,000 g and 4°C for 15 min to get rid of the unsolved debris. Concentration of the
715 supernatant was measured by BCA assay. Proteins in samples were separated by 6-12%
716 SDS-PAGE, transferred to a Immobilon-P Transfer Membrane (Millipore), and then
717 incubated with indicated primary antibodies diluted in blocking buffer at 4°C
718 overnight after blocking by 5% non-fat milk solution in TBST (50 mM Tris, pH 7.4,
719 150 mM NaCl, 0.1% Tween 20) for 1 hr at room temperature. The primary antibodies
720 used were: pErbB3 (1:2500, Abcam, ab133459), pErbB4 (1:2500, Abcam, ab109273),
721 pErbB2 (1:2500, Abgent, AP3781q), EGFR (1:5000, Epitomics, 1902-1), pEGFR
722 (1:2500, Epitomics, 1727-1), GAPDH (1:5000, Huabio, EM1101), MBP (1:1000,
723 Millipore, MAB382), Olig2 (1:1000, Millipore, MABN50), ErbB3 (1:200, Santa
724 Cruz Biotechnology, sc-285), ErbB4 (1:200, Santa Cruz Biotechnology, sc-283),
725 ErbB2 (1:200, Santa Cruz Biotechnology, sc-284), RIP3 (1:2000, QED, 2283),
726 MLKL (1:2000, Abgent, AP14272B). For antibodies against phosphorylated proteins,
727 10% fetal bovine serum was used as blocking buffer. Next day, the membranes were
728 washed by TBST for three times and incubated with the secondary antibodies for 1 hr
729 at room temperature. Membranes were washed again and incubated with Immobilon

730 Western Chemiluminescent HRPSubstrate (Millipore) for visualization of
731 chemiluminescence by exposure to X-ray films or Bio-Rad GelDOCXR^{+} Imaging
732 System. Intensities of protein bands were measured by Image J, and statistical
733 analysis was performed after subtraction of the background intensity and
734 normalization with controls in each batch of experiments.

735

736 ***In situ* hybridization**

737 RNA *in situ* hybridization was performed as previously described (*Schaeren-Wiemers*
738 *and Gerfin-Moser, 1993*) with minor modifications. Briefly, the 14 μm PFA-fixed
739 brain sections were post-fixed in 4% PFA in PBS for 20 min, incubated in 2 μg/mL
740 Proteinase K in 50 mM Tris-Cl (pH 7.4) with 5 mM EDTA at room temperature for
741 10 min, re-fixed in 4% PFA in PBS for another 10 min, and then acetylated in 1.33%
742 triethanolamine and 0.25% acetic anhydride solution at room temperature for 10 min.
743 The acetylated sections were washed and incubated in hybridization buffer (50%
744 formamide, 0.25 mg/mL yeast RNA, 0.5 mg/mL herring sperm DNA, 5x Denhard's,
745 5x SSC, Invitrogen) at room temperature for 1 hr, and then hybridized with 0.5 ng/μL
746 digoxigenin-labeled *Enpp6* riboprobe in hybridization buffer at 65°C for 16 hr. The
747 hybridized sections were washed three times in 0.2x SSC at 65°C for total 1 hr, and
748 then were blocked with 10% sheep serum (Sigma-Aldrich) in solution I containing
749 100 mM pH 7.5 Tris-Cl with 0.15 M NaCl at room temperature for 1 hr, followed by
750 incubation with alkaline phosphatase-conjugated anti-digoxigenin antibody (Roche)
751 in the same solution at 4°C overnight. After washing three times with solution I for
752 total 1 hr, and twice with developing buffer containing 100 mM pH 9.5 Tris-Cl, 0.1 M
753 NaCl, 50 mM $MgCl_2$ and 0.1% Tween-20, the sections were incubated with 2%

NBT/BCIP solution (Roche) in the developing buffer at room temperature in the dark. The reaction was stopped by immersing the sections in PBS with 5 mM EDTA when appropriate signals were detected. To obtain mouse *Enpp6* riboprobes, a 1.3 kb fragment corresponding to Enpp6 mRNA (1400–2700 nt of NM_177304.4) was cloned into pBluescript II KS(-). The linearized plasmids were used as templates for *in vitro* transcription with T3 RNA polymerase (Promega) according to the manufacturer's instructions.

Real-time reverse transcription-PCR (RT-PCR)

Total RNA was extracted from isolated mouse white matter using TRIzol following manufacturer's protocol. cDNA was synthesized by using the 5x All-In-One RT MasterMix (abmGood). Real-time PCR was performed in four repeats for each sample by using BrightGreen 2x qPCR MasterMix (abmGood) with the Bio-Rad CFX96 real-time PCR system as previously described (*Chen et al., 2017*). Relative mRNA levels were analyzed by software Bio-Rad CFX Manager 1.5. Transcripts of targeted genes were normalized to those of mouse 18S rRNA gene in the same samples. Primers for 18S rRNA were 5'-CGG ACA CGG ACA GGA TTG ACA and 5'-CCA GAC AAA TCG CTC CAC CAA CTA with a 94 bp PCR product. Primers for mouse EGFR gene and transgene dnEGFR were 5'-TCC TGC CAG AAT GTG AGC AG and 5'-ACG AGC TCT CTC TCT TGA AG with a 500 bp PCR product.

RNA-Seq Analyses

Subcortical white matter tissues isolated from *Sox10*-dnEGFR and littermate controls, or *Sox10*-ErbB2^{V664E} mice and littermate controls, were used (three pairs for each

group) for global transcriptome analysis by LC-Bio Co (Hangzhou, China). The final transcriptome was generated by Histat and StringTie. StringTie was used to estimate the expression level for mRNAs by calculating FPKM (Fragments Per Kilobase of exon model per Million mapped reads). Differentially expressed genes were identified by comparing FPKM of the mRNA reads from three sample pairs between *Sox10*-dnEGFR, or *Sox10*-ErbB2^{V664E} mice, and their littermate controls, by paired Student *t* test *via* MeV (MultiExperiment Viewer). Gene lists with significant difference ($P < 0.05$) in expression between *Sox10*-dnEGFR and littermate controls, or between *Sox10*-ErbB2^{V664E} and littermate controls, were compared, and genes with similar expression tendencies in *Sox10*-dnEGFR and *Sox10*-ErbB2^{V664E} mice were identified. Z value of these genes was calculated according to their FPKM by an equation "Z sample-i =[(log2(Signal sample-i)-Mean (Log2(Signal) of all samples)][Standard deviation (Log2(Signal) of all samples)]" and plotted as heat map by MeV. Gene Ontology (GO) term enrichment was analyzed by PANTHER Overrepresentation Test (Released 20171205) through http://geneontology.org with the significance estimated by Fisher's Exact Test (FDR, false discovery rate).

Behavioral Tests

Plp-ErbB2^{V664E} mice at P35 and *Sox10*-ErbB2^{V664E} mice at P30 after indicated Dox treatment were used in grid walking tests for motor function analysis. Behavioral analyses for *Sox10*-dnEGFR and littermate controls with Dox-feeding from P21, or *Plp*-dnEGFR mice and littermate controls with Dox-withdrawal from P21, were carried out with 12- to 16-week-old animals by investigators unaware of their genotypes. Tested mutant mice had littermate control mice with same sex. For PPI,

802 social interaction, eight-arm radial water maze, forced swim and tail suspension, all
803 tested mice were male. Animals were tested at a sequence of open field, social
804 interaction, rotarod, PPI, eight-arm radial water maze, and then forced swim and tail
805 suspension, to minimize the influence of stress on their behavioral performance.
806 There were 2-day gaps between tests.

807

808 **Open field** and **stereotyped behavior analysis**: Animals were placed in a chamber
809 (30 cm × 30 cm × 34.5 cm) and their movements were monitored and traced by a
810 tracking software EthoVision XT 12 (Noldus, The Netherland). Locomotive activity
811 was measured and summated at 5-min intervals over a 30-min period. Frequency and
812 cumulative duration of stereotyped behaviors observed during 30-min traveling in the
813 open field, including grooming, hopping, rearing supported, and sniffing, were
814 determined by EthoVision XT 12 and statistically analyzed. Anxiety of the animals
815 was assessed by the differences of time that they spent in the central zone and
816 peripheral zone during the 30 min.

817

818 **Rotarod**: To evaluate the sensorimotor coordination, mice were placed on an
819 accelerating rotarod (Mouse Rota-Rod NG, Harikul Science, UB47650, Italy) and
820 assessed for ability to maintain balance on the rotating bar that accelerated from 4 to
821 40 rpm over a 5-min period. Mice were tested for 4 trials in the first day with 30-min
822 gap between trials, and were tested for another 4 trials 24 hr later. Latency before fall
823 from the rod was recorded.

824

Prepulse inhibition (PPI) test: These tests were conducted in a sound-attenuated chamber (Panlab, LE116, Spain). Mice were placed in a Plexiglas restrainer mounted on a grid floor, and their startle responses were captured by a movement sensor and analyzed by a software Startle v1.2. Before the test, mice were allowed to habituate to the chamber with a 60 dB background white noise for 5 min, and to 4 times of auditory-evoked startle stimulating pulse (10000 Hz at 120 dB, 20 ms) with random 5-30 sec intervals. In the PPI test, mice were subjected to startle pulse trials (120 dB, 20 ms) or prepulse/pulse trials (20 ms 10000 Hz at 75, 80, or 85 dB with 100 ms interval before a 20 ms 120dB startle stimulus) with random 5-30 sec intervals between trials. Different trial types were presented randomly with each trial type presented 9-12 times, and no two consecutive trials were identical. Max startle response within 300 ms after onset of startle stimulus was recorded. PPI (%) was calculated according to the equation: [100 - (startle amplitude on prepulse-pulse trials/startle amplitude on pulse alone trials) ×100].

Social interaction: Mice were placed in a square chamber (50 cm × 50 cm × 50 cm) with two small transparent boxes at two opposite corners. The chamber was dark and mouse movement was monitored by infrared camera and traced by Anymaze software (Stoelting, Wood Dale, Illinois). After 5 min habituation in the chamber, mice were returned to their home cages. Mice were placed into the same chamber 2 hr later, with one of the boxes holding a stranger mouse that could be seen and smelled through multiple holes in the box. Social interaction ability of the tested mice was determined by their traveling distances in the quadrant with the stranger mouse as compared with the traveling distances in the quadrant with an empty box.

849

850 **Eight-arm radial water maze**: According to the previous report with modification
851 (*Penley et al., 2013*), animals were trained in eight-arm radial water maze for two
852 weeks, with four trials each day to search a hidden platform in each trial for escaping
853 from the water at 20-22 °C. Four hidden platforms were placed at the end of a same
854 set of arms for all the training and tests, as illustrated in Figure 7-figure supplement
855 1K. After a trial that mice reached a hidden platform, mice were returned to their
856 home cages with towel and warming pads. There was a 30-sec gap between trials, and
857 the visited platform was removed before the next trial. Mice aborted swimming
858 during training were discarded. Two weeks later, the trained mice were tested for their
859 working memory capacities that were represented by avoiding arms with visited
860 platforms in previous trials. In the last trial of the test day, the animals had highest
861 working memory load for they had to avoid swimming into three arms with platforms
862 removed. First and repeat entries into any arm that previously had a platform were
863 counted as working memory errors, and first entries into any arm that never had a
864 platform were counted as reference memory errors which represent deficits in spatial
865 recognition or long term memory. The day after test day, all the animals were tested
866 in a simple visible platform task with 5 trials in a round pool, and each trial contained
867 a visible platform placed at a different position 0.5-1.0 meter away from tested mice.
868 The latency of mice reached the visible platform in each trial was averaged to assess
869 their eyesight.

870

871 **Forced swim** and **Tail suspension**: In the forced swim test, mice were forced to swim
872 for 15 min in a cylinder with diameter at 11 cm, water depth at 30 cm and temperature

873 at 22-24 °C. One day later, mice were forced to swim again for 5 min in the same
874 cylinder and mouse movement was recorded and analyzed by Anymaze software. The
875 tail suspension test was carried out 2 days later after the forced swim test, in which
876 mice were suspended by using adhesive tape applied to the tail and videotaped for 5
877 min. Mouse movement during the 5 min was traced and analyzed by Anymaze
878 software. For both tests, immobile period was defined by 70% of mouse bodies were
879 motionless and lasted for at least 1 sec. Summation of immobile periods for each
880 mouse was taken into statistical analysis.

881

882 **Grid walking test**: Mice were placed on an elevated metal grid panel with each grid
883 cell 5 × 0.8 cm^2, and their movements were videotaped. The velocity of mouse
884 movement and percentage of foot-slip steps in total steps were calculated to assess
885 locomotor function of mice. Scores of foot slips reflect precise stepping, coordination
886 of the four limbs, and accurate paw placement, indicating ability of animals in
887 sensorimotor coordination.

888

889 **Electrophysiology**

890 Following anesthesia and decapitation, optic nerves were isolated from mice and
891 superfused with oxygenated artificial cerebrospinal fluid (ACSF) containing (in
892 mmol/L): 119 NaCl, 2.5 KCl, 2.5 CaCl2,1.3 MgCl2, 1.25 NaH2PO4, 26 NaHCO3,
893 and 10 glucose; pH 7.4. Optic nerve CAP recording methods were adopted and
894 modified from the previous reports (*Saab et al., 2016*). Briefly, two ends of the optic
895 nerves were attached by suction electrodes, which backfilled with ACSF and
896 connected to an IsoFlex (AMPI) for stimulation or a MultiClamp 700B (Molecular

Device) for recording. The recorded signal was amplified 50 times, filtered at 30 kHz, and acquired at 20-30 kHz. Data were collected and analyzed by pClamp 10.3 software (Molecular Devices). The optic nerves were equilibrated for at least 30 min in the perfusion chamber in normal ACSF at room temperature before experiments. All experiments were performed at room temperature.

Maximal CAP recording: For each recorded nerve, stimulus pulse (100 μs duration) strength was adjusted with a stepped increase and finally to evoke the maximal CAP. CAPs were elicited 5 times at every step of the stimulus strength. After reaching the maximal CAP, the stimulus was increased an additional 25% for supramaximal stimulation to ensure the activation of all axons in the nerve. Note the supramaximal stimulation did not further change the CAPs. The areas under CAPs were calculated to determine the nerve conduction.

Oxygen-glucose deprivation (OGD) assay: The assay was performed as previously described with modification (*Saab et al., 2016; Trevisiol et al., 2017*). During experiments, CAPs were evoked by the supramaximal stimulus every 20 sec. After 60-min stimulation of the baseline CAP in normal condition, OGD was induced for the nerves by switching bathing solution from oxygenated ACSF (saturated with 95% O2/5% CO2) to glucose-free ACSF (replaced with equimolar sucrose to maintain osmolarity) that was saturated with 95%N2/5%CO2. After 60-min OGD, oxygenated ACSF was restored and CAPs were recorded for another hour. CAPs recorded after 30-min baseline stimulation was taken as the initial CAPs. The effects of OGD on the

nerve conduction and recovery were determined by normalizing the areas of CAPs recorded during OGD or recovery sessions to that of initial CAPs.

Neural activity dependence assay: The protocol was modified from published reports (*Saab et al., 2016; Trevisiol et al., 2017*). Before the experiments, CAPs were recorded every 30 sec to obtain baseline with the stimulus pulse strength set at the supramaximal levels. To evaluate the conduction of optic nerves under increasing energy demands, we gradually increased the stimulating frequency from 1 to 100 Hz. Each stimulating frequency was applied for 30-60 sec. For 1 and 5 Hz stimuli, CAPs were continuously recorded and CAP areas were measured for each CAP. For 10 to 100 Hz, nerves were stimulated by a train of 100 stimuli, and rest for 1 sec before the next train of stimuli. CAP areas were sampled for the last four stimuli of each train and averaged as one data point. For the statistical analysis, CAP areas were normalized to the initial levels.

Statistical analysis

Statistical analyses other than for RNA-seq data (described separately above) were performed using Prism (Graphpad) and presented as mean ± s.e.m.. For western blotting and LFB staining results, statistical analyses were performed after subtraction of the background intensity and normalization with controls in each batch of experiments to minimize the influences of batch-to-batch variations. Two-tailed unpaired Student's *t* test was used for analysis between two groups with one variable, one-way ANOVA test was used for analysis among three or more groups with one variable, and two-way ANOVA test was used to determine difference among groups

with two variables. Statistical significance was set at $*P < 0.05$, $**P < 0.01$, $***P < 0.001$.

Data Availability

All data generated or analyzed during this study are included in the manuscript and supporting files. Source data files have been provided for all manuscript figures. Source data have been provided online at datadryad.org (https://doi.org/10.5061/dryad.jq2bvq87c). The accession number for the RNA-Seq data presented in this article is GEO: GSE123491.

Acknowledgements

We thank Wanwan He, Kaiwei Zhang, Youguang Yang, and Shasha Zhang in Hangzhou Normal University for the assistance in EM image analyses, and Dr. Wanhua Shen for the assistance in electrophysiological experiments. We also thank Dr. Woo-Ping Ge in UT Southwestern for comments on the manuscript.

This work was supported by grants from National Natural Science Foundation of China (31371075, 31671070, and 31871030 to YT).

Competing interests: The authors declare no competing interests.

965 # References

966 Aguirre A, Dupree JL, Mangin JM, and Gallo V. 2007. A functional role for EGFR
967 signaling in myelination and remyelination. *Nat Neurosci* **10**, 990-1002.
968 doi:10.1038/nn1938
969 Bergles DE, and Richardson WD. 2015. Oligodendrocyte Development and Plasticity.
970 *Cold Spring Harb Perspect Biol* **8**, a020453. doi:10.1101/cshperspect.a020453
971 Bradl M, and Lassmann H. 2010. Oligodendrocytes: biology and pathology. *Acta*
972 *Neuropathol* **119**, 37-53. doi:10.1007/s00401-009-0601-5
973 Brinkmann BG, Agarwal A, Sereda MW, Garratt AN, Muller T, Wende H, Stassart
974 RM, Nawaz S, Humml C, Velanac V, Radyushkin K, Goebbels S, Fischer TM,
975 Franklin RJ, Lai C, Ehrenreich H, Birchmeier C, Schwab MH, and Nave KA. 2008.
976 Neuregulin-1/ErbB signaling serves distinct functions in myelination of the peripheral
977 and central nervous system. *Neuron* **59**, 581-595. doi:10.1016/j.neuron.2008.06.028
978 Cai Z, Jitkaew S, Zhao J, Chiang HC, Choksi S, Liu J, Ward Y, Wu LG, and Liu ZG.
979 2014. Plasma membrane translocation of trimerized MLKL protein is required for
980 TNF-induced necroptosis. *Nat Cell Biol* **16**, 55-65. doi:10.1038/ncb2883
981 Chen J, He W, Hu X, Shen Y, Cao J, Wei Z, Luan Y, He L, Jiang F, and Tao Y. 2017. A
982 role for ErbB signaling in the induction of reactive astrogliosis. *Cell Discov* **3**, 17044.
983 doi:10.1038/celldisc.2017.44
984 Chong VZ, Thompson M, Beltaifa S, Webster MJ, Law AJ, and Weickert CS. 2008.
985 Elevated neuregulin-1 and ErbB4 protein in the prefrontal cortex of schizophrenic
986 patients. *Schizophrenia research* **100**, 270-280. doi:10.1016/j.schres.2007.12.474
987 Czopka T, Ffrench-Constant C, and Lyons DA. 2013. Individual oligodendrocytes
988 have only a few hours in which to generate new myelin sheaths in vivo. *Dev Cell* **25**,
989 599-609. doi:10.1016/j.devcel.2013.05.013
990 Douaud G, Smith S, Jenkinson M, Behrens T, Johansen-Berg H, Vickers J, James S,
991 Voets N, Watkins K, Matthews PM, and James A. 2007. Anatomically related grey
992 and white matter abnormalities in adolescent-onset schizophrenia. *Brain* **130**, 2375-
993 2386. doi:10.1093/brain/awm184
994 Fancy SP, Baranzini SE, Zhao C, Yuk DI, Irvine KA, Kaing S, Sanai N, Franklin RJ,
995 and Rowitch DH. 2009. Dysregulation of the Wnt pathway inhibits timely
996 myelination and remyelination in the mammalian CNS. *Genes Dev* **23**, 1571-1585.
997 doi:10.1101/gad.1806309
998 Fields RD. 2008. White matter in learning, cognition and psychiatric disorders. *Trends*

Neurosci **31**, 361-370.

Fu H, Cai J, Clevers H, Fast E, Gray S, Greenberg R, Jain MK, Ma Q, Qiu M, Rowitch DH, Taylor CM, and Stiles CD. 2009. A genome-wide screen for spatially restricted expression patterns identifies transcription factors that regulate glial development. *J Neurosci* **29**, 11399-11408. doi:10.1523/JNEUROSCI.0160-09.2009

Funfschilling U, Supplie LM, Mahad D, Boretius S, Saab AS, Edgar J, Brinkmann BG, Kassmann CM, Tzvetanova ID, Mobius W, Diaz F, Meijer D, Suter U, Hamprecht B, Sereda MW, Moraes CT, Frahm J, Goebbels S, and Nave KA. 2012. Glycolytic oligodendrocytes maintain myelin and long-term axonal integrity. *Nature* **485**, 517-521. doi:10.1038/nature11007

Futamura T, Toyooka K, Iritani S, Niizato K, Nakamura R, Tsuchiya K, Someya T, Kakita A, Takahashi H, and Nawa H. 2002. Abnormal expression of epidermal growth factor and its receptor in the forebrain and serum of schizophrenic patients. *Mol Psychiatry* **7**, 673-682. doi:10.1038/sj.mp.4001081

Guo F, Ma J, McCauley E, Bannerman P, and Pleasure D. 2009. Early postnatal proteolipid promoter-expressing progenitors produce multilineage cells in vivo. *J Neurosci* **29**, 7256-7270. doi:10.1523/JNEUROSCI.5653-08.2009

Hahn CG, Wang HY, Cho DS, Talbot K, Gur RE, Berrettini WH, Bakshi K, Kamins J, Borgmann-Winter KE, Siegel SJ, Gallop RJ, and Arnold SE. 2006. Altered neuregulin 1-erbB4 signaling contributes to NMDA receptor hypofunction in schizophrenia. *Nat Med* **12**, 824-828. doi:10.1038/nm1418

Hall J, Whalley HC, Job DE, Baig BJ, McIntosh AM, Evans KL, Thomson PA, Porteous DJ, Cunningham-Owens DG, Johnstone EC, and Lawrie SM. 2006. A neuregulin 1 variant associated with abnormal cortical function and psychotic symptoms. *Nat Neurosci* **9**, 1477-1478. doi:10.1038/nn1795

Harrington EP, Zhao C, Fancy SP, Kaing S, Franklin RJ, and Rowitch DH. 2010. Oligodendrocyte PTEN is required for myelin and axonal integrity, not remyelination. *Ann Neurol* **68**, 703-716. doi:10.1002/ana.22090

Harrison PJ, and Law AJ. 2006. Neuregulin 1 and schizophrenia: genetics, gene expression, and neurobiology. *Biol Psychiatry* **60**, 132-140. doi:10.1016/j.biopsych.2005.11.002

Hof PR, and Schmitz C. 2009. The quantitative neuropathology of schizophrenia. *Acta Neuropathol* **117**, 345-346. doi:10.1007/s00401-009-0495-2

Hoistad M, Segal D, Takahashi N, Sakurai T, Buxbaum JD, and Hof PR. 2009.

1033 Linking white and grey matter in schizophrenia: oligodendrocyte and neuron
1034 pathology in the prefrontal cortex. *Front Neuroanat* **3**, 9.
1035 doi:10.3389/neuro.05.009.2009
1036 Hughes EG, Orthmann-Murphy JL, Langseth AJ, and Bergles DE. 2018. Myelin
1037 remodeling through experience-dependent oligodendrogenesis in the adult
1038 somatosensory cortex. *Nat Neurosci* **21**, 696-706. doi:10.1038/s41593-018-0121-5
1039 Inamura N, Sugio S, Macklin WB, Tomita K, Tanaka KF, and Ikenaka K. 2012. Gene
1040 induction in mature oligodendrocytes with a PLP-tTA mouse line. *Genesis* **50**, 424-
1041 428. doi:10.1002/dvg.20808
1042 Ishii A, Furusho M, Dupree JL, and Bansal R. 2016. Strength of ERK1/2 MAPK
1043 Activation Determines Its Effect on Myelin and Axonal Integrity in the Adult CNS. *J*
1044 *Neurosci* **36**, 6471-6487. doi:10.1523/JNEUROSCI.0299-16.2016
1045 Iwakura Y, and Nawa H. 2013. ErbB1-4-dependent EGF/neuregulin signals and their
1046 cross talk in the central nervous system: pathological implications in schizophrenia
1047 and Parkinson's disease. *Front Cell Neurosci* **7**, 4. doi:10.3389/fncel.2013.00004
1048 Joshi D, Fullerton JM, and Weickert CS. 2014. Elevated ErbB4 mRNA is related to
1049 interneuron deficit in prefrontal cortex in schizophrenia. *Journal of psychiatric*
1050 *research* **53**, 125-132. doi:10.1016/j.jpsychires.2014.02.014
1051 Karlsgodt KH. 2020. White Matter Microstructure across the Psychosis Spectrum.
1052 *Trends Neurosci*. doi:10.1016/j.tins.2020.03.014
1053 Kelly S, Jahanshad N, Zalesky A, Kochunov P, Agartz I, Alloza C, Andreassen OA,
1054 Arango C, Banaj N, Bouix S, Bousman CA, Brouwer RM, Bruggemann J, Bustillo J,
1055 Cahn W, Calhoun V, Cannon D, Carr V, Catts S, Chen J, et al. 2018. Widespread white
1056 matter microstructural differences in schizophrenia across 4322 individuals: results
1057 from the ENIGMA Schizophrenia DTI Working Group. *Mol Psychiatry* **23**, 1261-
1058 1269. doi:10.1038/mp.2017.170
1059 Kessler RC, Amminger GP, Aguilar-Gaxiola S, Alonso J, Lee S, and Ustun TB. 2007.
1060 Age of onset of mental disorders: a review of recent literature. *Current opinion in*
1061 *psychiatry* **20**, 359-364. doi:10.1097/YCO.0b013e32816ebc8c
1062 Kougioumtzidou E, Shimizu T, Hamilton NB, Tohyama K, Sprengel R, Monyer H,
1063 Attwell D, and Richardson WD. 2017. Signalling through AMPA receptors on
1064 oligodendrocyte precursors promotes myelination by enhancing oligodendrocyte
1065 survival. *Elife* **6**. doi:10.7554/eLife.28080
1066 Kujala P, Portin R, and Ruutiainen J. 1997. The progress of cognitive decline in

multiple sclerosis. A controlled 3-year follow-up. *Brain* **120 (Pt 2)**, 289-297.

Law AJ, Lipska BK, Weickert CS, Hyde TM, Straub RE, Hashimoto R, Harrison PJ, Kleinman JE, and Weinberger DR. 2006. Neuregulin 1 transcripts are differentially expressed in schizophrenia and regulated by 5' SNPs associated with the disease. *Proceedings of the National Academy of Sciences of the United States of America* **103**, 6747-6752. doi:10.1073/pnas.0602002103

Law AJ, Wang Y, Sei Y, O'Donnell P, Piantadosi P, Papaleo F, Straub RE, Huang W, Thomas CJ, Vakkalanka R, Besterman AD, Lipska BK, Hyde TM, Harrison PJ, Kleinman JE, and Weinberger DR. 2012. Neuregulin 1-ErbB4-PI3K signaling in schizophrenia and phosphoinositide 3-kinase-p110delta inhibition as a potential therapeutic strategy. *Proc Natl Acad Sci U S A* **109**, 12165-12170. doi:10.1073/pnas.1206118109

Ludwig A, Schlierf B, Schardt A, Nave KA, and Wegner M. 2004. Sox10-rtTA mouse line for tetracycline-inducible expression of transgenes in neural crest cells and oligodendrocytes. *Genesis* **40**, 171-175. doi:10.1002/gene.20083

Luo X, He W, Hu X, and Yan R. 2014. Reversible overexpression of bace1-cleaved neuregulin-1 N-terminal fragment induces schizophrenia-like phenotypes in mice. *Biol Psychiatry* **76**, 120-127. doi:10.1016/j.biopsych.2013.09.026

Makinodan M, Rosen KM, Ito S, and Corfas G. 2012. A critical period for social experience-dependent oligodendrocyte maturation and myelination. *Science* **337**, 1357-1360. doi:10.1126/science.1220845

McIntosh AM, Moorhead TW, Job D, Lymer GK, Munoz Maniega S, McKirdy J, Sussmann JE, Baig BJ, Bastin ME, Porteous D, Evans KL, Johnstone EC, Lawrie SM, and Hall J. 2008. The effects of a neuregulin 1 variant on white matter density and integrity. *Mol Psychiatry* **13**, 1054-1059. doi:10.1038/sj.mp.4002103

Mei L, and Nave KA. 2014. Neuregulin-ERBB signaling in the nervous system and neuropsychiatric diseases. *Neuron* **83**, 27-49. doi:10.1016/j.neuron.2014.06.007

Nave KA, and Salzer JL. 2006. Axonal regulation of myelination by neuregulin 1. *Curr Opin Neurobiol* **16**, 492-500.

Nave KA, and Werner HB. 2014. Myelination of the nervous system: mechanisms and functions. *Annu Rev Cell Dev Biol* **30**, 503-533. doi:10.1146/annurev-cellbio-100913-013101

Oberst A, Dillon CP, Weinlich R, McCormick LL, Fitzgerald P, Pop C, Hakem R, Salvesen GS, and Green DR. 2011. Catalytic activity of the caspase-8-FLIP(L)

complex inhibits RIPK3-dependent necrosis. *Nature* **471**, 363-367. doi:10.1038/nature09852

Ofengeim D, Ito Y, Najafov A, Zhang Y, Shan B, DeWitt JP, Ye J, Zhang X, Chang A, Vakifahmetoglu-Norberg H, Geng J, Py B, Zhou W, Amin P, Berlink Lima J, Qi C, Yu Q, Trapp B, and Yuan J. 2015. Activation of necroptosis in multiple sclerosis. *Cell Rep* **10**, 1836-1849. doi:10.1016/j.celrep.2015.02.051

Palazuelos J, Crawford HC, Klingener M, Sun B, Karelis J, Raines EW, and Aguirre A. 2014. TACE/ADAM17 is essential for oligodendrocyte development and CNS myelination. *J Neurosci* **34**, 11884-11896. doi:10.1523/JNEUROSCI.1220-14.2014

Penley SC, Gaudet CM, and Threlkeld SW. 2013. Use of an eight-arm radial water maze to assess working and reference memory following neonatal brain injury. *J Vis Exp*, 50940. doi:10.3791/50940

Peters BD, and Karlsgodt KH. 2015. White matter development in the early stages of psychosis. *Schizophr Res* **161**, 61-69. doi:10.1016/j.schres.2014.05.021

Roy K, Murtie JC, El-Khodor BF, Edgar N, Sardi SP, Hooks BM, Benoit-Marand M, Chen C, Moore H, O'Donnell P, Brunner D, and Corfas G. 2007. Loss of erbB signaling in oligodendrocytes alters myelin and dopaminergic function, a potential mechanism for neuropsychiatric disorders. *Proc Natl Acad Sci U S A* **104**, 8131-8136.

Saab AS, Tzvetavona ID, Trevisiol A, Baltan S, Dibaj P, Kusch K, Mobius W, Goetze B, Jahn HM, Huang W, Steffens H, Schomburg ED, Perez-Samartin A, Perez-Cerda F, Bakhtiari D, Matute C, Lowel S, Griesinger C, Hirrlinger J, Kirchhoff F, et al. 2016. Oligodendroglial NMDA Receptors Regulate Glucose Import and Axonal Energy Metabolism. *Neuron* **91**, 119-132. doi:10.1016/j.neuron.2016.05.016

Schaeren-Wiemers N, and Gerfin-Moser AJH. 1993. A single protocol to detect transcripts of various types and expression levels in neural tissue and cultured cells: in situ hybridization using digoxigenin-labelled cRNA probes. *Histochemistry* **100**, 431-440. doi:10.1007/bf00267823

Schmucker J, Ader M, Brockschnieder D, Brodarac A, Bartsch U, and Riethmacher D. 2003. erbB3 is dispensable for oligodendrocyte development in vitro and in vivo. *Glia* **44**, 67-75.

Sun L, Wang H, Wang Z, He S, Chen S, Liao D, Wang L, Yan J, Liu W, Lei X, and Wang X. 2012. Mixed lineage kinase domain-like protein mediates necrosis signaling downstream of RIP3 kinase. *Cell* **148**, 213-227. doi:10.1016/j.cell.2011.11.031

Taveggia C, Thaker P, Petrylak A, Caporaso GL, Toews A, Falls DL, Einheber S, and

Salzer JL. 2008. Type III neuregulin-1 promotes oligodendrocyte myelination. *Glia* **56**, 284-293.

Ting AK, Chen Y, Wen L, Yin DM, Shen C, Tao Y, Liu X, Xiong WC, and Mei L. 2011. Neuregulin 1 promotes excitatory synapse development and function in GABAergic interneurons. *J Neurosci* **31**, 15-25. doi:10.1523/JNEUROSCI.2538-10.2011

Trevisiol A, Saab AS, Winkler U, Marx G, Imamura H, Mobius W, Kusch K, Nave KA, and Hirrlinger J. 2017. Monitoring ATP dynamics in electrically active white matter tracts. *Elife* **6**. doi:10.7554/eLife.24241

Tripathi RB, Jackiewicz M, McKenzie IA, Kougioumtzidou E, Grist M, and Richardson WD. 2017. Remarkable Stability of Myelinating Oligodendrocytes in Mice. *Cell Rep* **21**, 316-323. doi:10.1016/j.celrep.2017.09.050

Uranova NA, Vikhreva OV, Rachmanova VI, and Orlovskaya DD. 2011. Ultrastructural alterations of myelinated fibers and oligodendrocytes in the prefrontal cortex in schizophrenia: a postmortem morphometric study. *Schizophr Res Treatment* **2011**, 325789. doi:10.1155/2011/325789

Uranova NA, Vostrikov VM, Vikhreva OV, Zimina IS, Kolomeets NS, and Orlovskaya DD. 2007. The role of oligodendrocyte pathology in schizophrenia. *Int J Neuropsychopharmacol* **10**, 537-545. doi:10.1017/S1461145707007626

Watkins TA, Emery B, Mulinyawe S, and Barres BA. 2008. Distinct stages of myelination regulated by gamma-secretase and astrocytes in a rapidly myelinating CNS coculture system. *Neuron* **60**, 555-569. doi:10.1016/j.neuron.2008.09.011

Wegener A, Deboux C, Bachelin C, Frah M, Kerninon C, Seilhean D, Weider M, Wegner M, and Nait-Oumesmar B. 2015. Gain of Olig2 function in oligodendrocyte progenitors promotes remyelination. *Brain* **138**, 120-135. doi:10.1093/brain/awu375

Winterer G, Konrad A, Vucurevic G, Musso F, Stoeter P, and Dahmen N. 2008. Association of 5' end neuregulin-1 (NRG1) gene variation with subcortical medial frontal microstructure in humans. *Neuroimage* **40**, 712-718. doi:10.1016/j.neuroimage.2007.12.041

Woo RS, Li XM, Tao Y, Carpenter-Hyland E, Huang YZ, Weber J, Neiswender H, Dong XP, Wu J, Gassmann M, Lai C, Xiong WC, Gao TM, and Mei L. 2007. Neuregulin-1 enhances depolarization-induced GABA release. *Neuron* **54**, 599-610. doi:10.1016/j.neuron.2007.04.009

Xiao L, Ohayon D, McKenzie IA, Sinclair-Wilson A, Wright JL, Fudge AD, Emery B,

1169 Li H, and Richardson WD. 2016. Rapid production of new oligodendrocytes is
1170 required in the earliest stages of motor-skill learning. *Nat Neurosci* **19**, 1210-1217.
1171 doi:10.1038/nn.4351
1172 Ye F, Chen Y, Hoang T, Montgomery RL, Zhao XH, Bu H, Hu T, Taketo MM, van Es
1173 JH, Clevers H, Hsieh J, Bassel-Duby R, Olson EN, and Lu QR. 2009. HDAC1 and
1174 HDAC2 regulate oligodendrocyte differentiation by disrupting the beta-catenin-TCF
1175 interaction. *Nat Neurosci* **12**, 829-838. doi:10.1038/nn.2333
1176 Ying Z, Pan C, Shao T, Liu L, Li L, Guo D, Zhang S, Yuan T, Cao R, Jiang Z, Chen S,
1177 Wang F, and Wang X. 2018. Mixed Lineage Kinase Domain-like Protein MLKL
1178 Breaks Down Myelin following Nerve Injury. *Mol Cell* **72**, 457-468 e455.
1179 doi:10.1016/j.molcel.2018.09.011
1180 Zhang Y, Chen K, Sloan SA, Bennett ML, Scholze AR, O'Keeffe S, Phatnani HP,
1181 Guarnieri P, Caneda C, Ruderisch N, Deng S, Liddelow SA, Zhang C, Daneman R,
1182 Maniatis T, Barres BA, and Wu JQ. 2014. An RNA-sequencing transcriptome and
1183 splicing database of glia, neurons, and vascular cells of the cerebral cortex. *J Neurosci*
1184 **34**, 11929-11947. doi:10.1523/JNEUROSCI.1860-14.2014
1185 Zuliani R, Moorhead TW, Bastin ME, Johnstone EC, Lawrie SM, Brambilla P,
1186 O'Donovan MC, Owen MJ, Hall J, and McIntosh AM. 2011. Genetic variants in the
1187 ErbB4 gene are associated with white matter integrity. *Psychiatry research* **191**, 133-
1188 137. doi:10.1016/j.pscychresns.2010.11.001
1189
1190

Figure Legends:

Figure 1. ErbB overactivation in OLs induces demyelination in *Plp*-ErbB2^{V664E} (PB) mice but hypomyelination in *Sox10*-ErbB2^{V664E} (SB) mice. (**A** and **L**) Dox treatment setting for indicated mice and littermate controls. (**B** and **M**) Walking speed and percentage of foot slips of *Plp*-ErbB2^{V664E} mice and littermate controls (Ctrl) at P35 with 14 dpd, or *Sox10*-ErbB2^{V664E} mice and littermate controls at 9 dwd, in the grid walking test. Data were presented as mean ± s.e.m., and analyzed by two-tailed unpaired *t* test. n = 4 mice for each group. In B, for velocity, $t_{(6)} = 3.773$, $P = 0.0093$; For foot slips, $t_{(6)} = 12.31$, $P < 0.0001$. In M, for velocity, $t_{(6)} = 3.504$, $P = 0.0128$; For foot slips, $t_{(6)} = 4.429$, $P = 0.0044$. (**C** and **N**) Western blotting of indicated proteins in white matter tissues isolated from *Plp*-ErbB2^{V664E} mice, or *Sox10*-ErbB2^{V664E} mice, in comparison with that from littermate control mice. Activation status of each ErbB receptor was examined by western blotting with the specific antibody against its phosphorylated form. (**D** and **O**) Quantitative data of western blotting results were presented as mean ± s.e.m., and analyzed by two-tailed unpaired *t* test. In D, for EGFR, $t_{(4)} = 27.64$, $P < 0.0001$; for ErbB3, $t_{(4)} = 19.98$, $P < 0.0001$; for ErbB4, $t_{(4)} = 10.06$, $P = 0.0005$. In O, for EGFR, $t_{(4)} = 0.1983$, $P = 0.852$; for ErbB3, $t_{(4)} = 28.34$, $P < 0.0001$; for ErbB4, $t_{(4)} = 9.181$, $P = 0.00078$; for MBP, $t_{(4)} = 48.82$, $P < 0.0001$. (**E** and **P**) LFB staining results of coronal sections through the genu of the corpus callosum in *Plp*-ErbB2^{V664E} and littermate control mice, or in *Sox10*-ErbB2^{V664E} and littermate control mice. Black arrows indicate the lower staining intensity of myelin stained in the corpus callosum. (**F** and **Q**) Quantitative data for LFB staining intensity in the corpus callosum of indicated mice. Data were presented as mean ± s.e.m. and analyzed by two-tailed unpaired *t* test. In F, for the middle part at 9 dpd, $t_{(6)} = 6.345$, $P = 0.00072$; for the lateral part at 9 dpd, $t_{(6)} = 3.914$, $P = 0.0079$; for the middle part at

14 dpd, $t_{(6)} = 9.89$, $P < 0.0001$; for the lateral part at 14 dpd, $t_{(6)} = 23.07$, $P < 0.0001$. In Q, for the middle part, $t_{(6)} = 15.17$, $P < 0.0001$; for the lateral part, $t_{(6)} = 10.23$, $P < 0.0001$. (**G**) Western blotting results of MBP and ErbB2 in the cortex (CX) and the cerebellum (CE) isolated from *Plp*-ErbB2^{V664E} and littermate control mice at 14 dpd. GAPDH served as loading control. Quantitative data were presented as mean ± s.e.m., and analyzed by two-tailed unpaired *t* test. For CE, $t_{(4)} = 6.35$, $P = 0.0032$; for CX, $t_{(4)} = 9.243$, $P = 0.00076$. (**H** and **R**) The densities of myelinated axons examined by EM in different brain regions of *Plp*-ErbB2^{V664E} and littermate control mice at 14 dpd, or *Sox10*-ErbB2^{V664E} and littermate control mice at 9 dwd, were quantified. The percentages of axons with myelin breakdown were also quantified for *Plp*-ErbB2^{V664E} mice (H). CC, the corpus callosum; ON, the optic nerve; PFC, the prefrontal cortex. Data were presented as mean ± s.e.m., and analyzed by two-tailed unpaired *t* test. In H, for myelinated-axon density, in CC, $t_{(4)} = 2.863$, $P = 0.046$; in ON, $t_{(4)} = 1.818$, $P = 0.143$. For the percentage of axons with myelin breakdown, in CC, $t_{(4)} = 29.32$, $P < 0.0001$; in ON, $t_{(4)} = 6.108$, $P = 0.0036$; in PFC, $t_{(4)} = 8.125$, $P = 0.0012$. In R, for myelinated-axon density, in CC, $t_{(4)} = 0.2773$, $P = 0.795$; in ON, $t_{(4)} = 0.1455$, $P = 0.891$. (**I** and **S**) EM images of the corpus callosum (CC), optic nerve (ON), and prefrontal cortex (PFC) from *Plp*-ErbB2^{V664E} and littermate controls at 14 dpd, or from *Sox10*-ErbB2^{V664E} and littermate control mice at 9 dwd. Red arrow indicates the axon with myelin breakdown. Quantitative data were shown for *g*-ratio analysis of myelinated axons detected by EM. Averaged g-ratio for each mouse were plotted as inset, presented as mean ± s.e.m., and analyzed by two-tailed unpaired *t* test. In I, for CC, $t_{(4)} = 3.412$, $P = 0.027$; for ON, $t_{(4)} = 3.083$, $P = 0.037$; for PFC, $t_{(4)} = 7.11$, $P = 0.0021$. In S, for CC, $t_{(4)} = 3.295$, $P = 0.03$; for ON, $t_{(4)} = 3.775$, $P = 0.0195$; for PFC, $t_{(4)} = 1.196$, $P = 0.298$. (**J**, **K**, **T**, **U**) Astrocytes (GFAP^{+}) and microglia (Iba1^{+})

examined in the subcortical white matter of indicated mice by immunostaining. Cell densities in the corpus callosum were quantified, and data were presented as mean ± s.e.m., and analyzed by two-tailed unpaired *t* test. In J, $t_{(10)} = 4.753$, $P = 0.0008$. In K, $t_{(4)} = 36.4$, $P < 0.0001$. In T, $t_{(4)} = 0.0501$, $P = 0.962$. In U, $t_{(4)} = 1.637$, $P = 0.177$.

Figure 1-figure supplement 1. Expression of ErbB receptor members in white matter regions at different postnatal days. (**A**) Western blotting results of ErbB receptors in white matter regions isolated from wild type mice at different postnatal days. ns, non-specific band. (**B**) Quantitative data of the western blotting results were presented as mean ± s.e.m.. n = 3 independent experiments for each postnatal day. Data were normalized to P5 in each batch of experiments.

Figure 1-figure supplement 2. Unaltered myelin in the brains of *Plp*-tTA and *Sox10*$^{+/rtTA}$ mice, but hypermyelination at 9 dpd and axonal pathology at 14 dpd in *Plp*-ErbB2^{V664E} mice. (**A**) Representative EM images showed that myelin sheath ruptured and broke down in *Plp*-ErbB2^{V664E} mice at 14 dpd (red arrow). Note the associated nuclei (red asterisk) showed no chromatin condensation and nucleation. (**B**) Dramatically reduced axons in the subcortical white matter of *Plp*-ErbB2^{V664E} mice at 14 dpd. Sagittal sections of *Plp*-ErbB2^{V664E} (PB) and littermate control mice (Ctrl) were immunostained by monoclonal antibody TuJ1. Quantitative data were presented as mean ± s.e.m., and analyzed by two-tailed unpaired *t* test. $t_{(6)} = 6.019$, $P = 0.0009$. (**C**) EM images of the corpus callosum (CC) of *Plp*-tTA and littermate *TRE*-ErbB2^{V664E} mice at P35 with 14 dpd. *g*-ratio was calculated for myelinated axons. Averaged *g*-ratio (inset) were presented as mean ± s.e.m., and analyzed by two-tailed

unpaired *t* test. $t_{(4)} = 0.4472$, $P = 0.678$. (**D**) EM examination of axons in the midline of corpus callosum in *Plp*-ErbB2^{V664E} mice at 9 dpd. Note most axons remained intact despite that there were a few axons had myelin breakdown (red arrow). *g*-ratio was calculated for myelinated axons and averaged *g*-ratio for each mouse were analyzed by two-tailed unpaired *t* test (inset). $t_{(4)} = 3.226$, $P = 0.0321$. (**E**) The densities of myelinated axons as well as the percentages of axons with myelin breakdown in EM analysis of the midline of corpus callosum in *Plp*-ErbB2^{V664E} mice (PB) and littermate controls (Ctrl) at 9 dpd. Data were presented as mean ± s.e.m., and analyzed by two-tailed unpaired *t* test. For myelinated-axon density, $t_{(4)} = 0.805$, $P = 0.466$. For axons with myelin breakdown, $t_{(4)} = 3.567$, $P = 0.023$. (**F**) EM images of the corpus callosum of *Sox10*$^{+/rtTA}$ and littermate *TRE*-ErbB2^{V664E} mice at P30 with 9 dwd. *g*-ratio was calculated for myelinated axons. Averaged *g*-ratio (inset) were presented as mean ± s.e.m., and analyzed by two-tailed unpaired *t* test. $t_{(4)} = 0.3042$, $P = 0.776$.

Figure 2. *Plp*-tTA targets MOs whereas *Sox10*$^{+/rtTA}$ targets OPC-NFOs in mouse brains in late postnatal development. (**A**) Schematic illustration of stereotactic injection sites of AAV-*TRE*-YFP. (**B** and **C**) The percentage of Olig2^{+}YFP^{+}, CC1^{+}YFP^{+}, or PDGFRα^{+}YFP^{+} (NG2^{+}YFP^{+}) cells in YFP^{+} cells for indicated mice 1 (AAV-1d) or 2 days (AAV-2d) after AAV-*TRE*-YFP injection at P14 (B) or P35 (C). Data were from repeated immunostaining results of 3-7 mice for each group, presented as mean ± s.e.m., and analyzed by two-tailed unpaired *t* test. For *Plp*-tTA at P14 from AAV-1d to AAV-2d: Olig2^{+}YFP^{+} cells, $t_{(12)} = 0.3698$, $P = 0.718$; CC1^{+}YFP^{+} cells, $t_{(13)} = 0.5666$, $P = 0.581$; PDGFRα^{+}YFP^{+} cells, $t_{(10)} = 7.532$, $P <$

0.0001. For *Sox10*$^{+/rtTA}$ at P14 from AAV-1d to AAV-2d: Olig2^{+}YFP^{+} cells, $t_{(13)}$ = 0.2055, P = 0.840; CC1^{+}YFP^{+} cells, $t_{(8)}$ = 0.6425, P = 0.539; PDGFRα^{+}YFP^{+} cells, $t_{(5)}$ = 1.021, P = 0.354. For *Plp*-tTA at P35 from AAV-1d to AAV-2d: Olig2^{+}YFP^{+} cells, $t_{(17)}$ = 0.4959, P = 0.626; CC1^{+}YFP^{+} cells, $t_{(9)}$ = 2.32, P = 0.046; NG2^{+}YFP^{+} cells, $t_{(18)}$ = 1.003, P = 0.329. For *Sox10*$^{+/rtTA}$ at P35 from AAV-1d to AAV-2d: Olig2^{+}YFP^{+} cells, $t_{(11)}$ = 1.098, P = 0.296; CC1^{+}YFP^{+} cells, $t_{(23)}$ = 0.8614, P = 0.398; NG2^{+}YFP^{+} cells, $t_{(26)}$ = 7.869, P < 0.0001. (**D**) Immunostaining revealed that TCF4 was specifically expressed in a small fraction of Olig2^{+} cells, but not in PDGFRα^{+} cells, in the corpus callosum of mice at P30. Solid arrow, the representative double positive cell; Open arrow, the representative cell positive for TCF4 only. (**E** and **F**) Double immunostaining results of TCF4 and YFP for brain slices from indicated mice 1 (AAV-1d) or 2 days (AAV-2d) after virus injection at P14 (E) or P35 (F). Note that TCF4^{+} nuclei in AAV-infected area were almost all localized in YFP^{+} cells in *Sox10*$^{+/rtTA}$ mice 1 day after virus injection (AAV-1d) at either P14 or P35, and the colocalization reduced after 1 more day (AAV-2d). Solid arrows, representative double positive cells; Open arrows, representative cells positive for TCF4 only. (**G** and **H**) The percentage of TCF4^{+}YFP^{+} in YFP^{+} cells (G), and the density of TCF4^{+}YFP^{+} cells (H), were analyzed. Data were from repeated immunostaining results of 3-7 mice for each group, presented as mean ± s.e.m., and analyzed by two-tailed unpaired *t* test. For the percentage in *Sox10*$^{+/rtTA}$ mice from AAV-1d to AAV-2d: at P14, $t_{(10)}$ = 4.39, P = 0.0014; at P35, $t_{(28)}$ = 6.041, P < 0.0001. For the percentage in *Plp*-tTA mice from AAV-1d to AAV-2d: at P14, $t_{(26)}$ = 1.574, P = 0.128; at P35, $t_{(22)}$ = 2.367, P = 0.027. For the density in *Sox10*$^{+/rtTA}$ mice from AAV-1d to AAV-2d: at P14, $t_{(10)}$ = 5.685, P = 0.0002; at P35, $t_{(28)}$ = 4.813, P < 0.0001. For the density in *Plp*-tTA mice from AAV-1d to AAV-2d: at P14, $t_{(26)}$ = 1.581, P = 0.126; at

1314 P35, $t_{(22)}$ = 1.429, P = 0.167. (**I**) Schematic summary of OL stage-targeting
1315 preferences of *Plp*-tTA or *Sox10*$^{+/rtTA}$ during juvenile to adolescent development.

1316

1317 **Figure 2-figure supplement 1.** Targeting preferences on OPCs or post-mitotic OLs
1318 of *Plp*-tTA and *Sox10*$^{+/rtTA}$ from P14 to P35. (**A-D**) AAV-*TRE*-YFP was
1319 stereotactically injected into the corpus callosum of *Sox10*$^{+/rtTA}$ or *Plp*-tTA mice at
1320 P14 or P35. Brain sections obtained 1 (AAV-1d) or 2 (AAV-2d) days after virus
1321 injection were co-immunostained by antibodies to YFP and Olig2, or by CC1
1322 antibody and antibody to YFP, or by antibodies to YFP and NG2 (or PDGFRα).
1323 Shown are representative images for indicated mice at P14 or P35. *Sox10*$^{+/rtTA}$ mice
1324 were fed with Dox for 3 days before stereotactic injection of the virus, while *Plp*-tTA
1325 mice had no Dox treatment. (**E** and **F**) Distributions of infected cell, as shown by co-
1326 immunostaining of YFP and TCF4, in the corpus callosum of *Sox10*$^{+/rtTA}$ (E) or *Plp*-
1327 tTA (F) mice at P35. Note that infected cells in *Sox10*$^{+/rtTA}$ mice stringently
1328 distributed within TCF4^{+} cell clustered region, whereas those in *Plp*-tTA mice
1329 distributed broadly in the corpus callosum. Solid arrows, regions with clustered
1330 TCF4^{+} cells; Open arrows, regions with fewer TCF4^{+} cells.

1331

1332

1333 **Figure 3.** ErbB overactivation induces MO necroptosis in *Plp*-ErbB2^{V664E} (PB) mice
1334 but OPC apoptosis in *Sox10*-ErbB2^{V664E} (SB) mice. (**A** and **I**) Dox treatment setting
1335 for indicated mice and littermate controls. (**B**) The numbers of degenerating OLs
1336 (represented by nuclei associated with CC1^{+} cell debris, white arrows) increased in
1337 the corpus callosum of *Plp*-ErbB2^{V664E} mice starting from 6 dpd as revealed by CC1

immunostaining. (**C**) Quantitative data of intact $CC1^+$ density in *Plp*-ErbB2^{V664E} and control mice (Ctrl) with indicated Dox treatment were present as mean ± s.e.m., and analyzed by two-tailed unpaired *t* test. For 4 dpd, $t_{(4)} = 1.485$, $P = 0.212$; for 6 dpd, $t_{(4)} = 5.203$, $P = 0.0065$; for 9 dpd, $t_{(4)} = 20.95$, $P < 0.0001$. (**D** and **J**) Apoptotic cells (arrows) in the corpus callosum of *Plp*-ErbB2^{V664E} and control mice at 9 dpd (D), or *Sox10*-ErbB2^{V664E} and control mice at 9 dwd (J), were examined by TUNEL assays. Note the increased numbers of nuclei ($DAPI^+$) and non-specifically stained hemorrhagic spot (asterisk), which is the consequence of inflammation, in the brain slice of *Plp*-ErbB2^{V664E} mice (D). (**E**) Quantitative data of apoptotic cell densities in indicated mice. Data were presented as mean ± s.e.m., and analyzed by two-tailed unpaired *t* test. For PB, $t_{(6)} = 0.1128$, $P = 0.914$; for SB, $t_{(5)} = 8.344$, $P = 0.0004$. (**F** and **L**) Co-immunostaining results of MLKL or RIP3 with CC1 in the corpus callosum of indicated mice with indicated Dox treatments. (**G**) Western blotting results of MLKL and RIP3 in the white matter of *Plp*-ErbB2^{V664E} mice, or in that of *Sox10*-ErbB2^{V664E} mice, and in those of littermate control mice. ns, non-specific bands. (**H**) Quantitative data of immunostaining and western blotting results of MLKL or RIP3 in indicated mice at 9 days with Dox treatment. Data were presented as mean ± s.e.m., and analyzed by two-tailed unpaired *t* test. In western blotting results, for RIP3 protein in PB, $t_{(4)} = 3.579$, $P = 0.023$; for MLKL protein in PB, $t_{(4)} = 13.69$, $P= 0.00017$. In immunostaining results, for percentage of $RIP3^+$ in $CC1^+$ cells in PB, $t_{(4)} = 6.002$, $P = 0.0039$; for percentage of $MLKL^+$ in $CC1^+$ cells in PB, $t_{(4)} = 8.202$, $P = 0.0012$. (**K**) Apoptotic cells ($TUNEL^+$) were OPCs ($NG2^+$) in *Sox10*-ErbB2^{V664E} mice at P30 with 9 dwd. Arrows, representative double positive cells. Note OPCs in *Sox10*-ErbB2^{V664E} mice were hypertrophic. The percentage of

1362 TUNEL^{+}NG2^{+} cells in NG2^{+} cells were quantified and data were presented as mean ±
1363 s.e.m. and analyzed by two-tailed unpaired *t* test. $t_{(4)} = 3.95$, $P = 0.0168$.

1364

1365 **Figure 3-figure supplement 1.** Pathological OL proliferation in subcortical white
1366 matter of *Plp*-ErbB2^{V664E} mice. (**A**) Dramatically increased Olig2^{+} and NG2^{+} cells in
1367 the subcortical white matter of *Plp*-ErbB2^{V664E} mice at 14 dpd. Sagittal sections of
1368 *Plp*-ErbB2^{V664E} and littermate control mice were immunostained by antibodies for
1369 Olig2 or NG2. (**B** and **D**) Immunostaining results of NG2 and TCF4 (B), Olig2 with
1370 Ki67 (D), in the corpus callosum of indicated mice. (**C** and **E**) Quantitative data of
1371 immunostaining results in *Plp*-ErbB2^{V664E} (PB) and control mice (Ctrl) with indicated
1372 Dox treatment were present as mean ± s.e.m., and analyzed by two-tailed unpaired *t*
1373 test. For TCF4^{+} density at 9 dpd, $t_{(15)} = 2.1$, $P = 0.053$. For Olig2^{+} density: at 4 dpd, $t_{(6)}$
1374 $= 0.2923$, $P = 0.780$; at 6 dpd, $t_{(6)} = 3.16$, $P = 0.0196$; at 9 dpd, $t_{(4)} = 8.563$, $P = 0.001$.
1375 For NG2^{+} density at 9 dpd, $t_{(4)} = 9.912$, $P = 0.0006$. For Olig2^{+}Ki67^{+} density: at 4 dpd,
1376 $t_{(4)} = 1.187$, $P = 0.301$; at 6 dpd, $t_{(4)} = 3.428$, $P = 0.027$; at 9 dpd, $t_{(4)} = 8$, $P = 0.0013$.

1377

1378

1379 **Figure 4.** ErbB inhibition induces hypomyelination in *Sox10*-dnEGFR (SE) mice, but
1380 no myelin alteration in *Plp*-dnEGFR (PE) mice. (**A** and **F**) Dox treatment setting for
1381 indicated mice and littermate controls. (**B** and **G**) MBP levels and the inhibited
1382 phosphorylation in ErbB receptors were examined by western blotting in the white
1383 matter of *Sox10*-dnEGFR mice, or *Plp*-dnEGFR mice, in comparison with that of
1384 littermate controls (Ctrl). (**C** and **H**) Quantitative data of western blotting results. Data
1385 were presented as mean ± s.e.m., and analyzed by two-tailed unpaired *t* test. In C at

P35, for EGFR, $t_{(4)} = 1.813$, $P = 0.144$; for ErbB3 , $t_{(4)} = 25.94$, $P < 0.0001$; for ErbB4, $t_{(4)} = 12.69$, $P = 0.00022$; for MBP, $t_{(4)} = 0.7711$, $P = 0.484$. In C at P65, for EGFR, $t_{(4)} = 35.09$, $P < 0.0001$; for ErbB3, $t_{(4)} = 0.3492$, $P = 0.745$; for ErbB4, $t_{(4)} = 0.138$, $P = 0.897$; for MBP, $t_{(4)} = 4.842$, $P = 0.0084$. In H at P35, for EGFR, $t_{(4)} = 28.36$, $P < 0.0001$; for ErbB3, $t_{(4)} = 4.925$, $P = 0.0079$; for ErbB4, $t_{(4)} = 8.838$, $P = 0.0009$; for MBP, $t_{(4)} = 0.00896$, $P = 0.993$. In H at P65, for EGFR, $t_{(4)} = 43.97$, $P < 0.0001$; for ErbB3, $t_{(4)} = 5.157$, $P = 0.0067$; for ErbB4, $t_{(4)} = 44.67$, $P < 0.0001$; for MBP, $t_{(4)} = 0.4686$, $P = 0.664$. (**D** and **I**) LFB staining results of coronal sections through the genu of the corpus callosum in *Sox10*-dnEGFR and control mice at P65 with 44 dwd (D), or *Plp*-dnEGFR and control mice at P65 with 44 dpd (I). Black arrows indicate the middle part of the corpus callosum in *Sox10*-dnEGFR mice exhibiting obvious lower staining intensity. Quantitative data of LFB intensity were presented as mean ± s.e.m., and analyzed by two-tailed unpaired *t* test. In D, for the middle part, $t_{(6)} = 21.18$, $P < 0.0001$; for the lateral part, $t_{(6)} = 9.121$, $P < 0.0001$. In I, for the middle part, $t_{(4)} = 1.814$, $P = 0.144$; for the lateral part, $t_{(4)} = 0.0287$, $P = 0.979$. (**E** and **J**) EM images of the corpus callosum (CC), optic nerve (ON), and prefrontal cortex (PFC) from *Sox10*-dnEGFR and littermate controls at 44 dwd (E), or *Plp*-dnEGFR and littermate controls at 44 dpd (J). *g*-ratio was calculated for myelinated axons and averaged *g*-ratio were analyzed by two-tailed unpaired *t* test (inset). In E, for CC, $t_{(4)} = 2.793$, $P = 0.0383$; for ON, $t_{(7)} = 2.629$, $P = 0.0339$; for PFC, $t_{(4)} = 0.8697$, $P = 0.434$. In J, for CC, $t_{(4)} = 0.1139$, $P = 0.915$; for ON, $t_{(4)} = 0.0754$, $P = 0.944$; for PFC, $t_{(4)} = 0.6334$， $P = 0.561$.

Figure 4-figure supplement 1. No myelin alteration in *Sox10*-dnEGFR (SE) or *Plp*-dnEGFR (PE) mice at P35 with 14 days of Dox treatment. (**A** and **D**) Dox treatment

setting for indicated mice and littermate controls. (**B** and **E**) Without an antibody recognizing dnEGFR specifically, we examined the expression of dnEGFR/EGFR by real-time RT-PCR. As *Sox10*$^{+/rtTA}$ targets a transient cellular stage, transcripts of dnEGFR/EGFR in the subcortical white matter of *Sox10*-dnEGFR mice were only 4- and 9-fold more than that of the endogenous EGFR in littermate controls (Ctrl) at P35 and P65, respectively, while that of *Plp*-dnEGFR mice were 90- and 24-fold more than the endogenous EGFR transcripts in littermate controls at P35 and P65, respectively. Data were presented as mean ± s.e.m., and analyzed by two-tailed unpaired *t* test. For *Sox10*-dnEGFR at P35, $t_{(10)} = 5.044$, $P = 0.0005$; at P65, $t_{(10)} = 8.531$, $P < 0.0001$. For *Plp*-dnEGFR at P35, $t_{(10)} = 4.908$, $P = 0.0006$; at P65, $t_{(10)} = 4.515$, $P = 0.0011$. (**C** and **F**) EM images of the corpus callosum (CC), optic nerve (ON), and prefrontal cortex (PFC) from *Sox10*-dnEGFR and littermate controls at P35 with 14 dwd, or from *Plp*-dnEGFR and littermate controls at P35 with 14 dpd. *g*-ratio was calculated for myelinated axons. Averaged *g*-ratio for each mouse (inset) were presented as mean ± s.e.m., and analyzed by two-tailed unpaired *t* test. In C, for CC, $t_{(4)} = 0.1013$, $P = 0.924$; for ON, $t_{(4)} = 0.6191$, $P = 0.569$; for PFC, $t_{(4)} = 0.02485$, $P = 0.981$. In F, for CC, $t_{(4)} = 0.1443$, $P = 0.892$; for ON, $t_{(4)} = 0.01551$, $P = 0.988$; for PFC, $t_{(4)} = 0.1573$, $P = 0.883$.

Figure 5. ErbB activation negatively regulates OPC proliferation. (**A-C**) Statistic results of Olig2$^+$, CC1$^+$, and NG2$^+$ cell densities in the corpus callosum of *Sox10*-ErbB2^{V664E} mice (SB) and littermate controls (Ctrl) at P30 with 9 dwd, *Sox10*-dnEGFR mice (SE) and littermate controls at P65 with 44 dwd, or *Plp*-dnEGFR mice

(PE) and littermate controls at P65 with 44 dpd. Data were from repeated immunostaining of 3 mice for each group, presented as mean ± s.e.m., and analyzed by two-tailed unpaired *t* test. In A, for $Olig2^+$, $t_{(4)} = 6.236$, $P = 0.0034$; for $CC1^+$, $t_{(4)} = 16.92$, $P < 0.0001$; for $NG2^+$, $t_{(4)} = 3.634$, $P = 0.0221$. In B, for $Olig2^+$, $t_{(10)} = 5.08$, $P = 0.0005$; for $CC1^+$, $t_{(4)} = 3.134$, $P = 0.0351$; for $NG2^+$, $t_{(17)} = 6.387$, $P < 0.0001$. In C, for $Olig2^+$, $t_{(10)} = 1.106$, $P = 0.295$; for $CC1^+$, $t_{(4)} = 0.9848$, $P = 0.381$; for $NG2^+$, $t_{(9)} = 1.062$, $P = 0.316$. (**D-F**) Double immunostaining results of Olig2 and Ki67 in the corpus callosum of indicated mice at indicated ages. Arrows, representative double positive nuclei. (**G**) Statistic results of densities of proliferating OL lineage cells ($Olig2^+Ki67^+$) examined in indicated mice at indicated ages. Data were from immunostaining of 3-4 mice for each group, presented as mean ± s.e.m., and analyzed by two-tailed unpaired *t* test. For *Sox10*-$ErbB2^{V664E}$ (SB) and control mice (Ctrl), $t_{(4)} = 3.924$, $P = 0.0172$. For *Sox10*-dnEGFR (SE) and Ctrl, at P35, $t_{(6)} = 0.5042$, $P = 0.632$; at P65, $t_{(6)} = 2.963$, $P = 0.0252$. For *Plp*-dnEGFR (PE) and Ctrl, at P35, $t_{(4)} = 0.1136$, $P = 0.9151$; at P65, $t_{(4)} = 0.6191$, $P = 0.569$. (**H** and **I**) Apoptotic cells ($TUNEL^+$, white arrows) in the corpus callosum of *Sox10*-dnEGFR mice (H), or *Plp*-dnEGFR mice (I), were as few as that in littermate controls at indicated ages.

Figure 5-figure supplement 1. ErbB inhibition in OPC-NFOs increases OL numbers. (**A-C**) $Olig2^+$, $CC1^+$, and $NG2^+$ cells in the corpus callosum of indicated mice at indicated ages were examined by immunostaining. Statistic results in (A) showed $Olig2^+$, $CC1^+$, and $NG2^+$ cell densities were similar in the corpus callosum of $Sox10^{+/rtTA}$ and littermate *TRE*-$ErbB2^{V664E}$ mice at P30 (9 dwd). Data were from immunostaining of 3 mice for each group, presented as mean ± s.e.m., and analyzed

1459 by two-tailed unpaired *t* test. For Olig2$^+$, $t_{(4)}$ = 1.418, P = 0.229; for CC1$^+$, $t_{(7)}$ =
1460 0.3431, P = 0.742; for NG2$^+$, $t_{(4)}$ = 1.394, P = 0.236.

1461

1462 **Figure 5-figure supplement 2.** No changes in OL numbers or proliferation in *Sox10*-
1463 dnEGFR or *Plp*-dnEGFR mice at P35 with 14 days of Dox treatment. (**A** and **D**)
1464 Statistic results of Olig2$^+$, CC1$^+$, and NG2$^+$ cell densities in the corpus callosum of
1465 indicated mice at P35. Data were from repeated immunostaining of 3 mice for each
1466 group, presented as mean ± s.e.m., and analyzed by one-way ANOVA. In A, for
1467 Olig2$^+$, $F_{(2,6)}$ = 1.651, P = 0.268; for CC1$^+$, $F_{(2,6)}$ = 0.8605, P = 0.469; for NG2$^+$, $F_{(2,17)}$
1468 = 1.624, P = 0.226. In D, for Olig2$^+$, $F_{(2,6)}$ = 1.054, P = 0.405; for CC1$^+$, $F_{(2,6)}$ =
1469 0.2694, P = 0.773; for NG2$^+$, $F_{(2,12)}$ = 1.633, P = 0.236. (**B** and **E**) Immunostaining
1470 results of Olig2$^+$, CC1$^+$, and NG2$^+$ cells in the corpus callosum of indicated mice at
1471 P35. (**C** and **F**) Double immunostaining results of Olig2 and Ki67 in the corpus
1472 callosum of indicated mice at P35. Arrows, representative double positive nuclei.

1473

1474

1475 **Figure 6.** ErbB activation positively regulates NFO differentiation. (**A**) RNA-seq was
1476 performed for white matter tissues isolated from *Sox10*-ErbB2^{V664E} mice at P30 with 9
1477 dwd, or *Sox10*-dnEGFR mice at P35 with 14 dwd, and their littermate controls. For
1478 each mouse group we sequenced three pairs of samples and identified 2298 genes that
1479 had altered expression in the white matter of *Sox10*-ErbB2^{V664E} mice (Figure 6-Source
1480 data 1), as well as 1184 genes in that of *Sox10*-dnEGFR mice (Figure 6-Source data 2).
1481 By comparing the two groups of genes, 68 genes with similar expression tendencies in
1482 the white matter of *Sox10*-ErbB2^{V664E} (soxEb *vs* treEb) and *Sox10*-dnEGFR (soxEG

vs treEG) mice were identified. Heat maps of Z value of each gene are presented. The raw RNA-seq data have been deposited in the GEO and SRA database and can be found at GEO: GSE123491. (**B-D**) *In situ* hybridization results of *Enpp6* in the corpus callosum of *Sox10*-ErbB2^{V664E} mice (B), *Sox10*-dnEGFR mice (C), or *Plp*-dnEGFR mice (D), and their littermate controls at indicated ages. (**E**) Statistic results of *Enpp6*$^{+}$ cell densities examined in indicated mice at indicated ages. Data were from repeated experiments of 3 mice for each group, presented as mean ± s.e.m., and analyzed by two-tailed unpaired *t* test. For *Sox10*-ErbB2^{V664E} mice (SB) and control mice (Ctrl) at P30, $t_{(12)} = 4.638$, $P = 0.0006$. For *Sox10*-dnEGFR mice (SE) and Ctrl, at P35, $t_{(9)} = 2.704$, $P = 0.024$; at P65, $t_{(7)} = 0.8322$, $P = 0.433$. For *Plp*-dnEGFR mice (PE) and Ctrl, at P35, $t_{(10)} = 3.45$, $P = 0.0062$; at P65, $t_{(6)} = 0.7724$, $P = 0.469$. (**F-H**) Immunostaining results of TCF4 in the corpus callosum of *Sox10*-ErbB2^{V664E} mice (F), *Sox10*-dnEGFR (G), or *Plp*-dnEGFR (H), with their littermate controls at indicated ages. (**I**) Statistic results of TCF4^{+} cell densities examined in indicated mice at indicated ages. Data were from repeated experiments of 3 mice for each group, presented as mean ± s.e.m., and analyzed by two-tailed unpaired *t* test. For *Sox10*-ErbB2^{V664E} mice (SB) and control mice (Ctrl) at P27, $t_{(4)} = 3.883$, $P = 0.0178$. For *Sox10*-dnEGFR mice (SE) and Ctrl, at P35, $t_{(6)} = 4.107$, $P = 0.006$; at P65, $t_{(6)} = 0.1948$, $P = 0.852$. For *Plp*-dnEGFR mice (PE) and Ctrl, at P35, $t_{(6)} = 6.776$, $P = 0.0005$; at P65, $t_{(6)} = 0.7845$, $P = 0.463$. (**J**) Ratio of TCF4^{+} to CC1^{+} cell numbers in indicated mice at indicated ages. Data were from 3 mice for each group, presented as mean ± s.e.m., and analyzed by two-tailed unpaired *t* test. For *Sox10*-dnEGFR mice (SE) at P35, $t_{(4)} = 4.251$, $P = 0.0131$; for *Plp*-dnEGFR mice (PE) at P35, $t_{(4)} = 7.762$, $P = 0.0015$; for *Sox10*-ErbB2^{V664E} (SB) mice at P27, $t_{(4)} = 3.322$, $P = 0.029$.

Figure 7. ErbB inhibition in MOs suppresses axonal conduction under energy stress and impairs working memory in the absence of myelin alteration. (**A** and **C**) Rotarod test, n = 12 mice for *Sox10*-dnEGFR and n = 12 mice for controls (two-way ANOVA test, $F_{(1, 176)} = 7.824$, $P = 0.0057$), while n = 12 mice for *Plp*-dnEGFR and n = 13 mice for controls (two-way ANOVA test, $F_{(1, 184)} = 1.4$, $P = 0.238$). (**B** and **D**) Open field tests, n = 13 mice for *Sox10*-dnEGFR and n = 11 mice for controls (two-way ANOVA test, $F_{(1, 132)} = 6.302$, $P = 0.013$), while n = 14 mice for *Plp*-dnEGFR and n = 19 mice for controls (two-way ANOVA test, $F_{(1, 186)} = 12.17$, $P = 0.0006$). (**E** and **F**) Eight-arm radial water maze test, n = 12 mice for *Sox10*-dnEGFR and n = 7 mice for controls (for working memory error, two-way ANOVA test, $F_{(1, 68)} = 6.334$, $P = 0.014$; for reference memory error, two-way ANOVA test, $F_{(1, 68)} = 0.0423$, $P = 0.838$; for visible platform, two-tailed unpaired *t* test, $t_{(17)} = 1.137$, $P = 0.271$), while n = 14 mice for *Plp*-dnEGFR and n = 10 mice for controls (for working memory error, two-way ANOVA test, $F_{(1, 88)} = 4.782$, $P = 0.0314$; for reference memory error, two-way ANOVA test, $F_{(1, 88)} = 0.498$, $P = 0.482$; for visible platform, two-tailed unpaired *t* test, $t_{(22)} = 0.8254$, $P = 0.418$). Data were presented as mean ± s.e.m.. In illustrative examples of the travel pathways of indicated mice, green circles indicate the last arms with a hidden platform, while red crosses indicate the arms with used platforms in the past three trials. (**G** and **H**) Axonal excitability is similar in *Plp*-dnEGFR optic nerves and control nerves (G), but decreased in *Sox10*-dnEGFR optic nerves in comparison with controls (H). CAPs of optic nerves generated by electrical stimuli with intensities at stepped increase (0-0.2 mA) were recorded *ex vivo*. Data were from 3-7 optic nerves of 3-5 mice for each group, presented as mean ± s.e.m., and analyzed by two-way ANOVA. In G, $F_{(1, 202)} = 0.2118$, $P = 0.646$. In H, $F_{(1, 139)} = 102.1$, $P < 0.0001$.

Representative maximal CAPs for each group are shown at the left. (**I** and **J**) The CAP decline induced by OGD is slightly accelerated and aggravated in *Plp*-dnEGFR optic nerves (I), but decelerated and attenuated in *Sox10*-dnEGFR optic nerves (J). OGD was started for the recorded nerves after 1-hr baseline stimulation, and stopped after another hour by restoring the bathing media to oxygenated ACSF. Initial CAPs were recorded after 30-min baseline stimulation. The areas under CAPs were measured and normalized to the initial levels. Data were from 4-8 optic nerves of 3-5 mice for each group, presented as mean ± s.e.m., and analyzed by two-way ANOVA. In I, for baseline, $F_{(1, 1572)} = 320.7$, $P < 0.0001$; for OGD, $F_{(1, 2280)} = 47.95$, $P < 0.0001$; for recovery, $F_{(1, 2040)} = 5.896$, $P = 0.015$. In J, for baseline, $F_{(1, 732)} = 87.06$, $P < 0.0001$; for OGD, $F_{(1, 1140)} = 196.6$, $P < 0.0001$; for recovery, $F_{(1, 1020)} = 173.1$, $P < 0.0001$. (**K** and **L**) Neuronal activities with frequency at 5-100Hz increased the CAP decline in *Plp*-dnEGFR optic nerves (K), but increased the CAPs at 10-25Hz and slowed the CAP decline at 50-100Hz in *Sox10*-dnEGFR optic nerves (L), in comparison with their controls, respectively. Data were from 4-8 optic nerves of 3-5 mice for each group, presented as mean ± s.e.m., and analyzed by two-way ANOVA. In K, for 1Hz, $F_{(1, 270)} = 0.076$, $P = 0.783$; for 5Hz, $F_{(1, 1044)} = 147.5$, $P < 0.0001$; for 10Hz, $F_{(1, 27)} = 17.64$, $P = 0.0003$; for 25Hz, $F_{(1, 54)} = 14.26$, $P = 0.0004$; for 50Hz, $F_{(1, 90)} = 19.82$, $P < 0.0001$; for 100Hz, $F_{(1, 135)} = 52.82$, $P < 0.0001$. In L, for 1Hz, $F_{(1, 390)} = 52.7$, $P < 0.0001$; for 5Hz, $F_{(1, 1508)} = 4.194$, $P = 0.041$; for 10Hz, $F_{(1, 39)} = 8.352$, $P = 0.0063$; for 25Hz, $F_{(1, 78)} = 50.46$, $P < 0.0001$; for 50Hz, $F_{(1, 130)} = 46.3$, $P < 0.0001$; for 100Hz, $F_{(1, 195)} = 19.59$, $P < 0.0001$. (**M**) Schematic illustration of the pathophysiological consequences induced by ErbB receptor dysregulation in different OL stages as well as the pathogenic mechanisms (emphasized in brown).

Figure 7-figure supplement 1. No behavioral abnormalities in sensory gating, social interaction, or mood behaviors revealed for *Sox10*-dnEGFR or *Plp*-dnEGFR mice. Behavioral performance of adult *Sox10*-dnEGFR mice with littermate controls (A-E), or *Plp*-dnEGFR mice with littermate controls (F-J), were tested in the open field test (**A** and **F**), social interaction test (**B** and **G**), prepulse inhibition (PPI) test (**C** and **H**), stereotyped behaviors in the open field (**D** and **I**), and the forced swim test and the tail suspension test (**E** and **J**). For zone analysis of open field tests, n = 13 mice for *Sox10*-dnEGFR and n = 11 mice for controls (two-way ANOVA test, $F_{(1, 44)} = 0$, $P > 0.9999$), while n = 14 mice for *Plp*-dnEGFR and n = 19 mice for controls (two-way ANOVA test, $F_{(1, 62)} = 0.00017$, $P = 0.989$). For PPI tests, n = 12 mice for *Sox10*-dnEGFR and n = 10 mice for controls (two-way ANOVA test, $F_{(1, 60)} = 2.36$, $P = 0.13$), while n = 12 mice for *Plp*-dnEGFR and n = 14 mice for controls (two-way ANOVA test, $F_{(1, 72)} = 0.9134$, $P = 0.342$). For social interaction tests, n = 13 mice for *Sox10*-dnEGFR and n = 12 mice for controls (two-way ANOVA test, $F_{(1, 46)} = 0.027$, $P = 0.87$), while n = 13 mice for *Plp*-dnEGFR and n = 14 mice for controls (two-way ANOVA test, $F_{(1, 50)} = 0.1023$, $P = 0.75$). For forced swim and tail suspension tests, n = 13 mice for *Sox10*-dnEGFR and n = 10 mice for controls (two-tailed unpaired *t* test, for forced swim, $t_{(21)} = 0.1799$, $P = 0.859$; for tail suspension, $t_{(21)} = 0.2576$, $P = 0.799$), while n = 13 mice for *Plp*-dnEGFR and n = 13 mice for controls (two-tailed unpaired *t* test, for forced swim, $t_{(24)} = 0.2676$, $P = 0.791$; for tail suspension, $t_{(24)} = 1.189$, $P = 0.246$). Data were presented as mean ± s.e.m.. Note that only male mice were used for PPI, social interaction, forced swim and tail suspension tests. (**K**) Illustration showing the setting for eight-arm radial water maze. Four hidden platforms were placed at the end of a same set of arms with 38-cm distance to the central zone at the training and test days. Mice started swimming with face to the arm

1583 end from No.1 arm in each trial, and the visited platform was removed before the next
1584 trial after 30-sec gap.

1585

1586 **Other Supplemental Files:**

1587 **Figure 7-Video 1.** The performances recorded for *Sox10*-dnEGFR mice and *Plp*-
1588 dnEGFR mice, as well as their controls, in the 4th trial of eight arm radial water maze
1589 at the test day.

1590 **Figure 6-Source data 1.** The Excel file contains the processed RNA-seq results of
1591 genes with differential expression in white matter tissues between *Sox10*-ErbB2^{V664E}
1592 mice and littermate *TRE*-ErbB2^{V664E} mice at P30 with 9 dwd.

1593 **Figure 6-Source data 2.** The Excel file contains the processed RNA-seq results of
1594 genes with differential expression in white matter tissues between *Sox10*-dnEGFR
1595 mice and littermate *TRE*-dnEGFR mice at P35 with 14 dwd.

1596 **Source data for graphs.** The zip file includes all raw numerical data in Prism files
1597 for graphs in each figure.

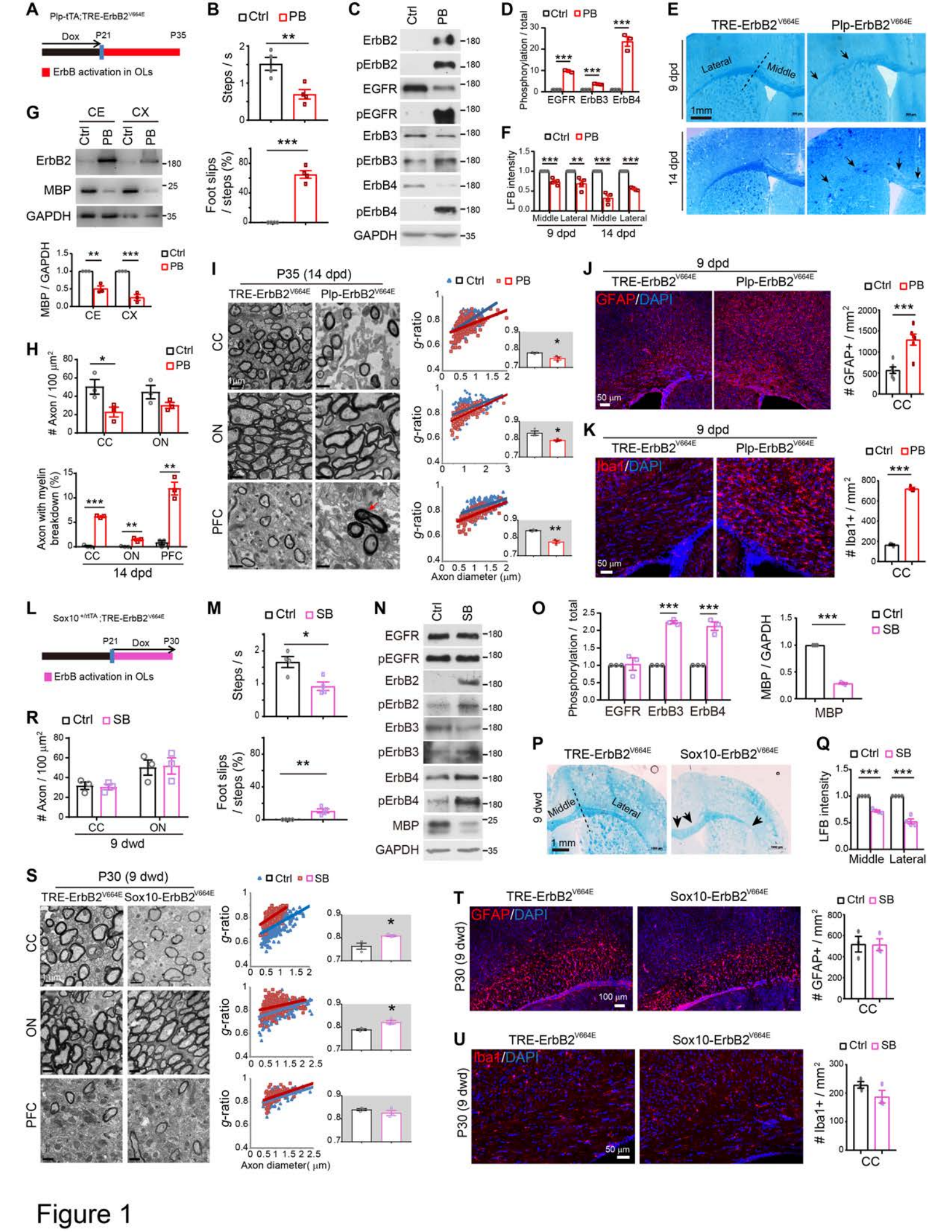
A
Plp-tTA;TRE-ErbB2V664E
Dox
P21
P35
ErbB activation in OLs
B
Ctrl
PB
Steps / s
Foot slips / steps (%)
C
ErbB2
pErbB2
EGFR
pEGFR
ErbB3
pErbB3
ErbB4
pErbB4
GAPDH
D
Phosphorylation / total
EGFR
ErbB3
ErbB4
E
TRE-ErbB2V664E
Plp-ErbB2V664E
9 dpd
14 dpd
Lateral
Middle
1mm
F
LFB intensity
Middle
Lateral
9 dpd
14 dpd
G
CE
CX
MBP
MBP / GAPDH
H
Axon / 100 μm2
Axon with myelin breakdown (%)
CC
ON
PFC
14 dpd
I
P35 (14 dpd)
g-ratio
Axon diameter (μm)
J
GFAP/DAPI
GFAP+ / mm2
50 μm
K
Iba1/DAPI
Iba1+ / mm2
L
Sox10+/rtTA;TRE-ErbB2V664E
P21
Dox
P30
ErbB activation in OLs
M
SB
N
O
MBP
P
Sox10-ErbB2V664E
9 dwd
1 mm
Q
R
9 dwd
S
P30 (9 dwd)
T
P30 (9 dwd)
100 μm
U
50 μm

Figure 1

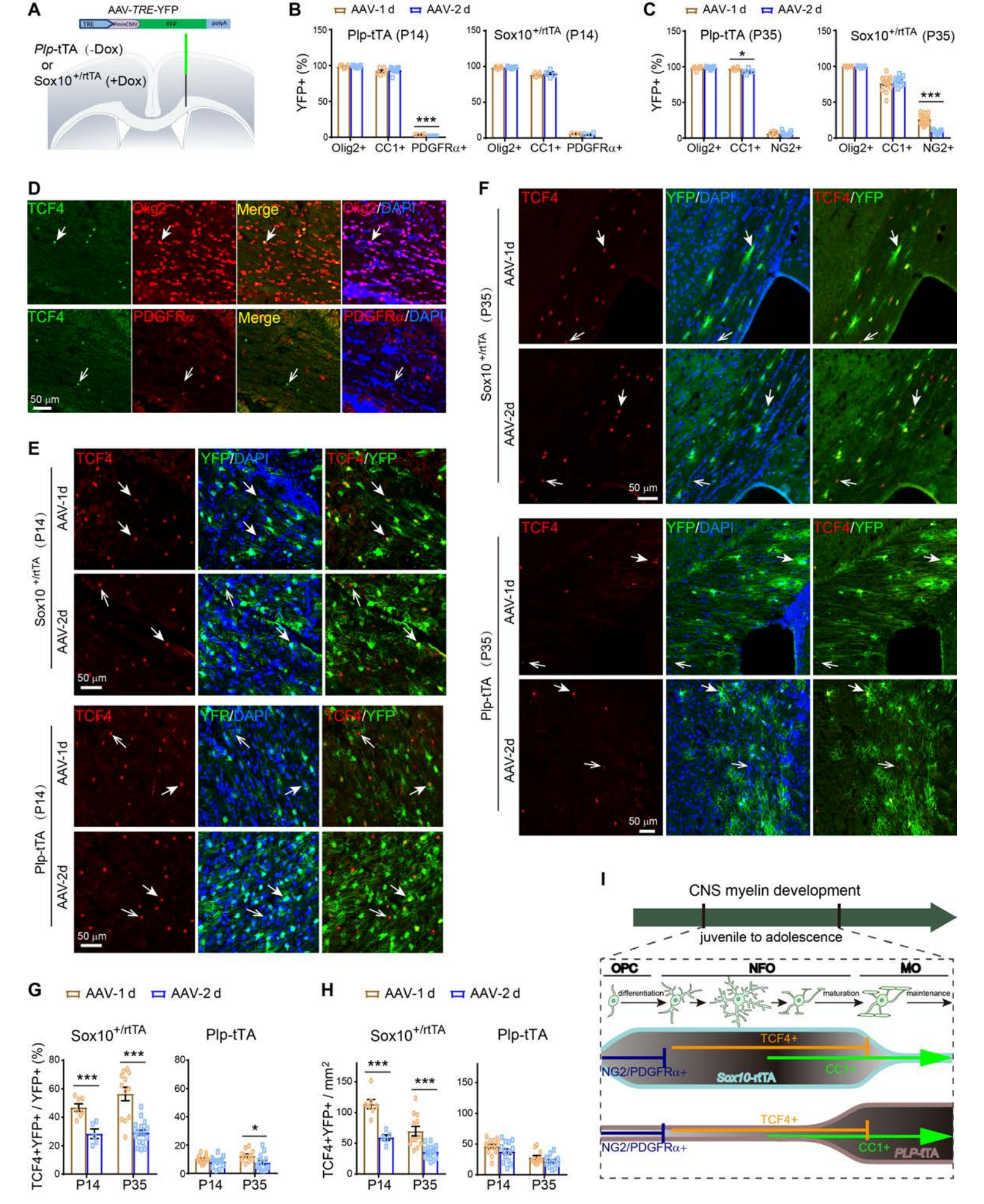
A
AAV-TRE-YFP
TRE
YFP
polyA
Plp-tTA (-Dox)
or
Sox10+/rtTA (+Dox)
B
AAV-1 d
AAV-2 d
Plp-tTA (P14)
Sox10+/rtTA (P14)
YFP+ (%)
Olig2+
CC1+
PDGFRα+
C
Plp-tTA (P35)
Sox10+/rtTA (P35)
NG2+
D
TCF4
Olig2
Merge
Olig2/DAPI
PDGFRα
PDGFRα/DAPI
50 μm
E
Sox10 +/rtTA (P14)
Plp-tTA (P14)
AAV-1d
AAV-2d
YFP/DAPI
TCF4/YFP
F
Sox10 +/rtTA (P35)
Plp-tTA (P35)
G
TCF4+YFP+ / YFP+ (%)
P14
P35
H
TCF4+YFP+ / mm2
I
CNS myelin development
juvenile to adolescence
OPC
NFO
MO
differentiation
maturation
maintenance
TCF4+
NG2/PDGFRα+
Sox10-rtTA
CC1+
PLP-tTA

Figure 2

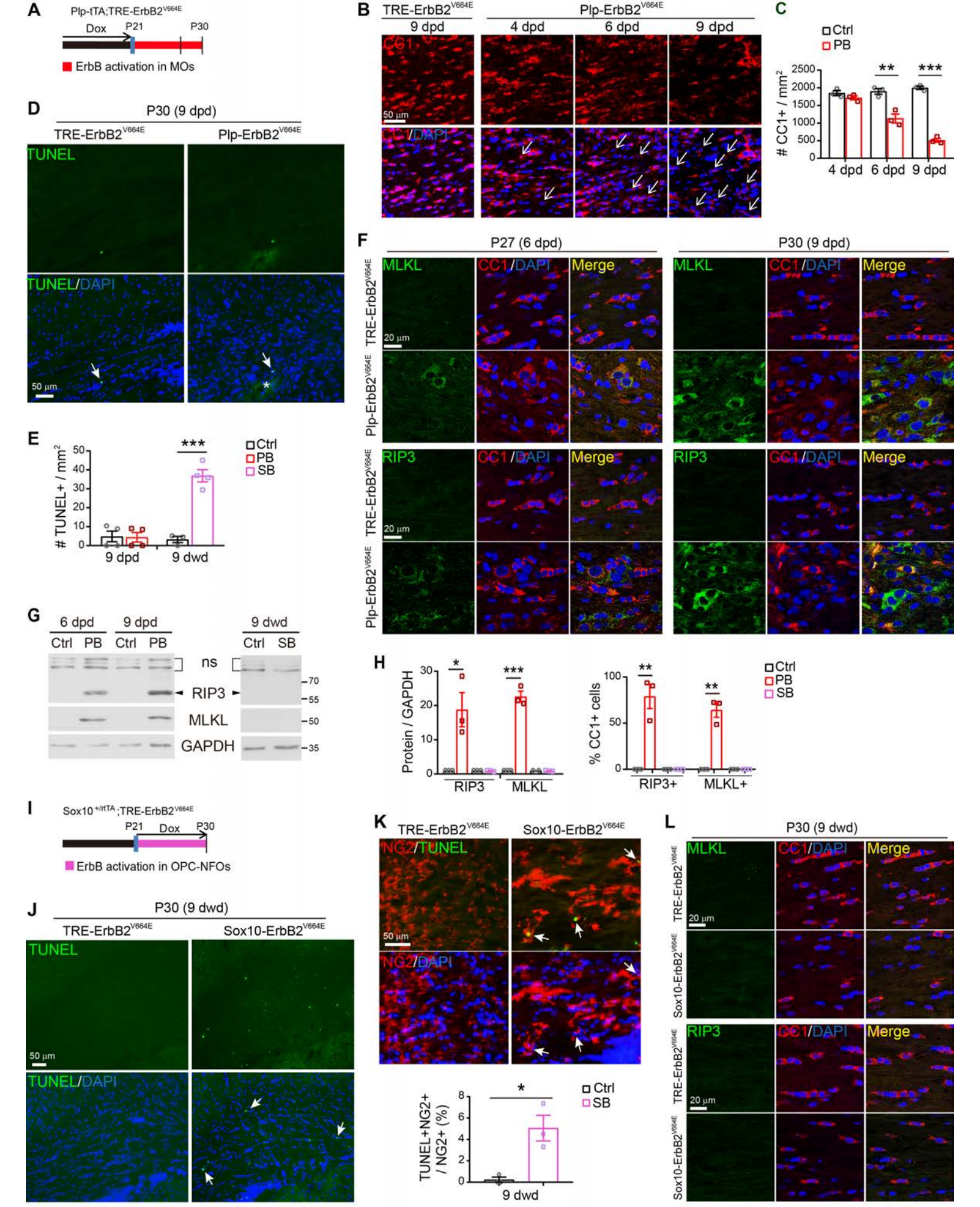
A
Plp-tTA;TRE-ErbB2V664E
Dox
P21
P30
ErbB activation in MOs
B
TRE-ErbB2V664E
Plp-ErbB2V664E
9 dpd
4 dpd
6 dpd
9 dpd
CC1
CC1/DAPI
50 μm
C
Ctrl
PB
CC1+ / mm2
2500
2000
1500
1000
500
0
**
***
4 dpd
6 dpd
9 dpd
D
P30 (9 dpd)
TRE-ErbB2V664E
Plp-ErbB2V664E
TUNEL
TUNEL/DAPI
50 μm
E
TUNEL+ / mm2
50
40
30
20
10
0
***
Ctrl
PB
SB
9 dpd
9 dwd
F
P27 (6 dpd)
P30 (9 dpd)
TRE-ErbB2V664E
Plp-ErbB2V664E
MLKL
CC1/DAPI
Merge
RIP3
20 μm
G
6 dpd
9 dpd
9 dwd
Ctrl
PB
SB
ns
RIP3
MLKL
GAPDH
70
55
50
35
H
Protein / GAPDH
30
20
10
0
*
***
RIP3
MLKL
% CC1+ cells
100
50
0
**
**
RIP3+
MLKL+
Ctrl
PB
SB
I
Sox10+/rtTA;TRE-ErbB2V664E
P21
Dox
P30
ErbB activation in OPC-NFOs
J
P30 (9 dwd)
TRE-ErbB2V664E
Sox10-ErbB2V664E
TUNEL
TUNEL/DAPI
50 μm
K
TRE-ErbB2V664E
Sox10-ErbB2V664E
NG2/TUNEL
NG2/DAPI
50 μm
TUNEL+NG2+ / NG2+ (%)
8
6
4
2
0
*
Ctrl
SB
9 dwd
L
P30 (9 dwd)
TRE-ErbB2V664E
Sox10-ErbB2V664E
MLKL
CC1/DAPI
Merge
RIP3
20 μm

Figure 3

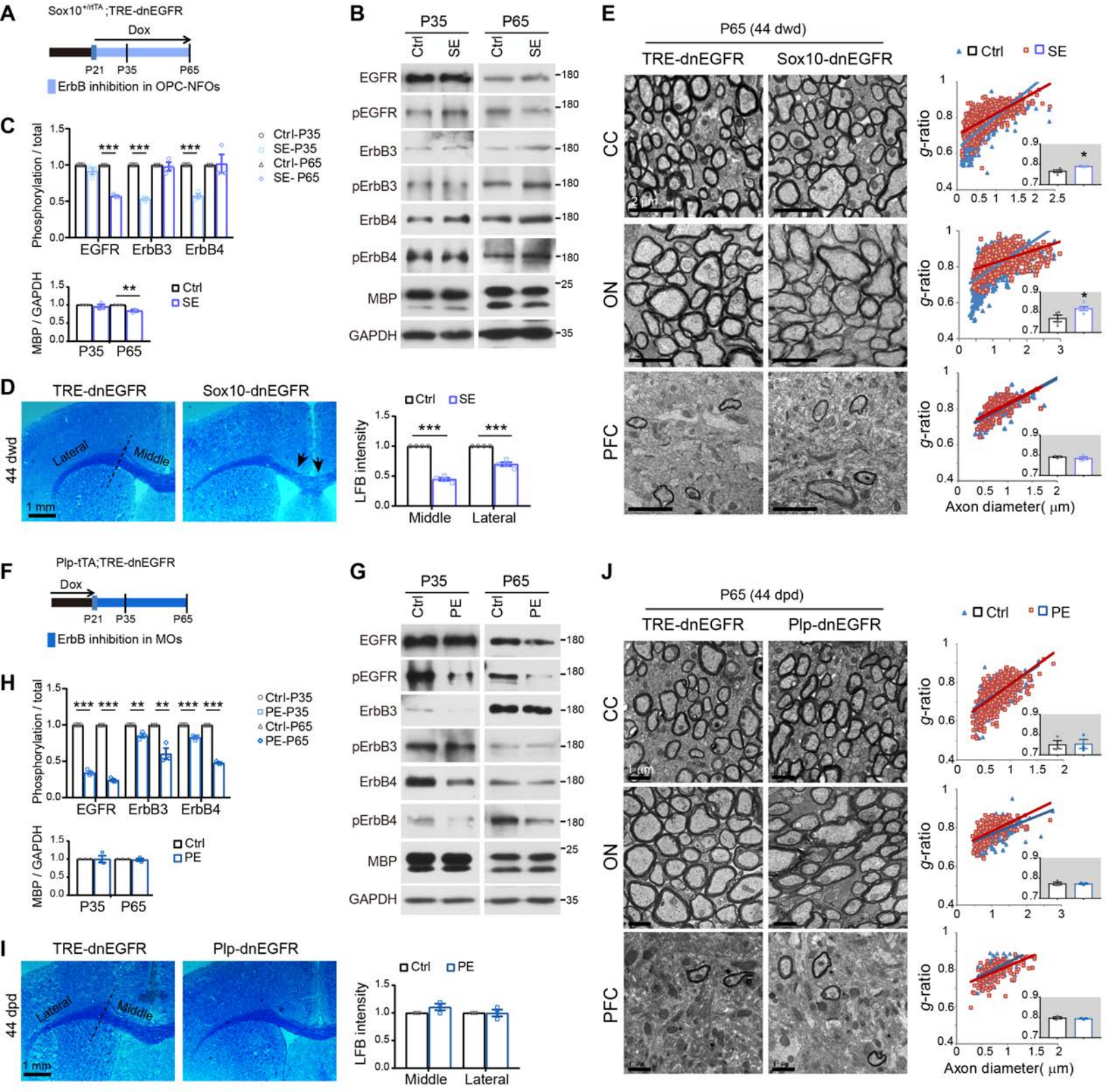
A
Sox10+/rtTA;TRE-dnEGFR
Dox
P21
P35
P65
ErbB inhibition in OPC-NFOs
B
P35
P65
Ctrl
SE
EGFR
pEGFR
ErbB3
pErbB3
ErbB4
pErbB4
MBP
GAPDH
C
Phosphorylation / total
Ctrl-P35
SE-P35
Ctrl-P65
SE- P65
EGFR
ErbB3
ErbB4
MBP / GAPDH
Ctrl
SE
D
TRE-dnEGFR
Sox10-dnEGFR
44 dwd
Lateral
Middle
1 mm
LFB intensity
Middle
Lateral
E
P65 (44 dwd)
TRE-dnEGFR
Sox10-dnEGFR
CC
ON
PFC
g-ratio
Axon diameter(μm)
F
Plp-tTA;TRE-dnEGFR
ErbB inhibition in MOs
G
PE
H
Ctrl-P35
PE-P35
Ctrl-P65
PE-P65
I
Plp-dnEGFR
44 dpd
J
P65 (44 dpd)
Plp-dnEGFR

Figure 4

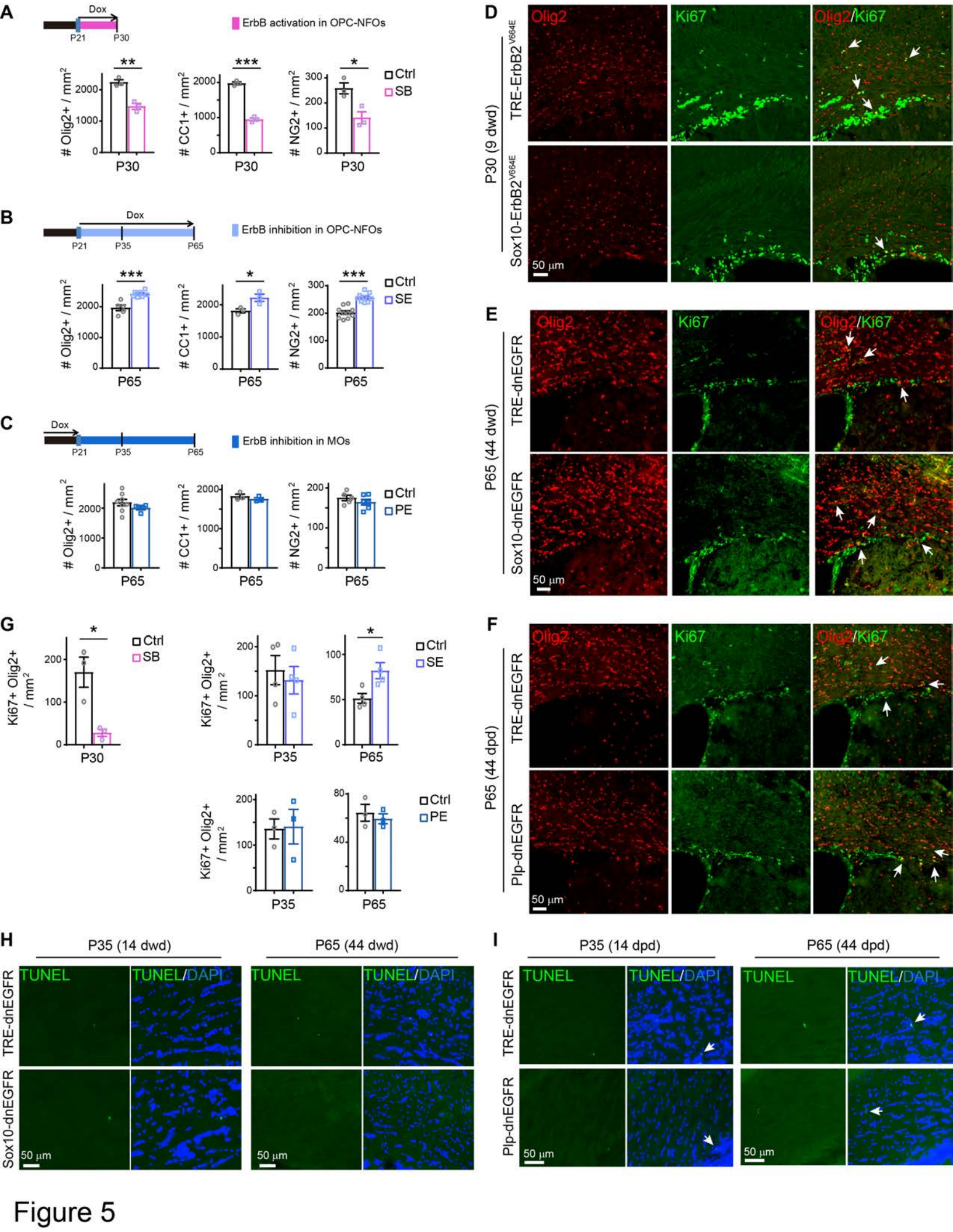
A
Dox
P21
P30
ErbB activation in OPC-NFOs
Olig2+ / mm2
CC1+ / mm2
NG2+ / mm2
P30
Ctrl
SB
B
Dox
P21
P35
P65
ErbB inhibition in OPC-NFOs
P65
Ctrl
SE
C
Dox
P21
P35
P65
ErbB inhibition in MOs
P65
Ctrl
PE
D
Olig2
Ki67
Olig2/Ki67
P30 (9 dwd)
TRE-ErbB2V664E
Sox10-ErbB2V664E
50 μm
E
Olig2
Ki67
Olig2/Ki67
P65 (44 dwd)
TRE-dnEGFR
Sox10-dnEGFR
50 μm
F
Olig2
Ki67
Olig2/Ki67
P65 (44 dpd)
TRE-dnEGFR
Plp-dnEGFR
50 μm
G
Ki67+ Olig2+ / mm2
P30
P35
P65
Ctrl
SB
SE
PE
H
P35 (14 dwd)
P65 (44 dwd)
TUNEL
TUNEL/DAPI
TRE-dnEGFR
Sox10-dnEGFR
50 μm
I
P35 (14 dpd)
P65 (44 dpd)
TUNEL
TUNEL/DAPI
TRE-dnEGFR
Plp-dnEGFR
50 μm

Figure 5

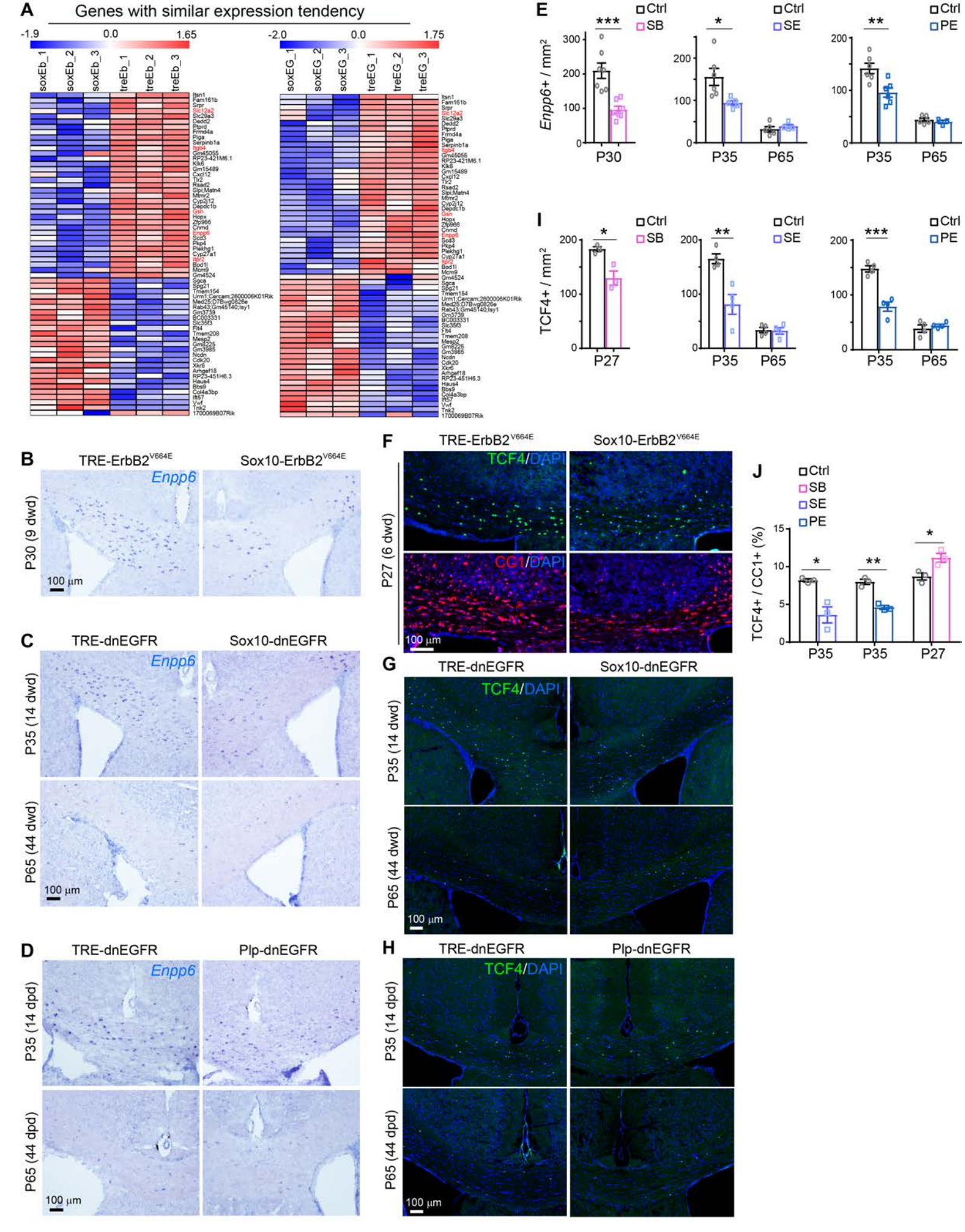
A
Genes with similar expression tendency
-1.9
0.0
1.65
soxEb_1
soxEb_2
soxEb_3
treEb_1
treEb_2
treEb_3
-2.0
0.0
1.75
soxEG_1
soxEG_2
soxEG_3
treEG_1
treEG_2
treEG_3
E
Enpp6+ / mm2
Ctrl
SB
SE
PE
P30
P35
P65
I
TCF4+ / mm2
P27
B
TRE-ErbB2V664E
Sox10-ErbB2V664E
Enpp6
P30 (9 dwd)
100 μm
C
TRE-dnEGFR
Sox10-dnEGFR
P35 (14 dwd)
P65 (44 dwd)
D
Plp-dnEGFR
P35 (14 dpd)
P65 (44 dpd)
F
TCF4/DAPI
CC1/DAPI
P27 (6 dwd)
G
H
J
TCF4+ / CC1+ (%)

Figure 6

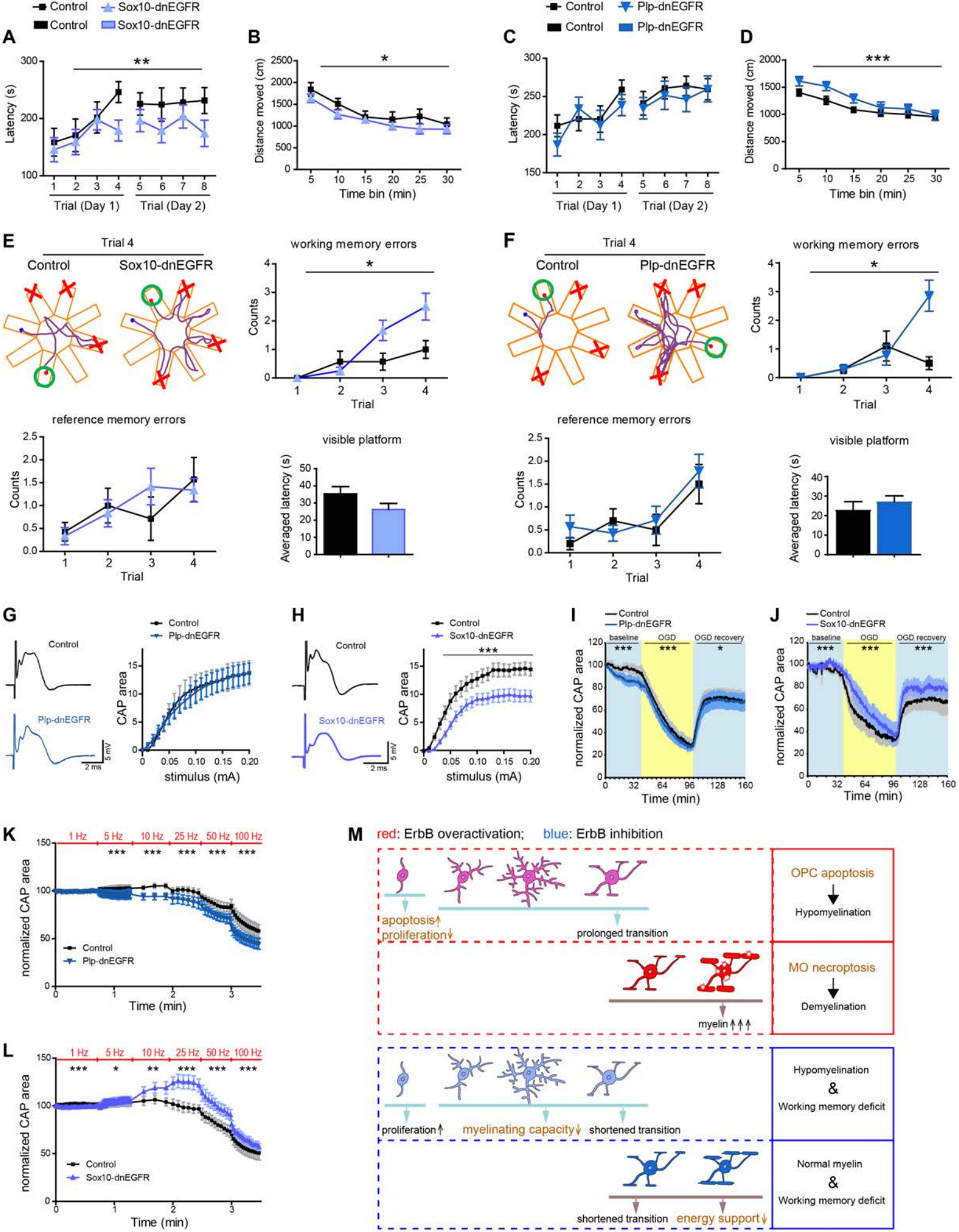
A
Control
Sox10-dnEGFR
Latency (s)
Trial (Day 1)
Trial (Day 2)
B
Distance moved (cm)
Time bin (min)
C
Plp-dnEGFR
D
E
Trial 4
working memory errors
reference memory errors
visible platform
Counts
Trial
Averaged latency (s)
F
G
CAP area
stimulus (mA)
H
I
normalized CAP area
baseline
OGD
OGD recovery
Time (min)
J
K
1 Hz
5 Hz
10 Hz
25 Hz
50 Hz
100 Hz
L
M
red: ErbB overactivation;
blue: ErbB inhibition
apoptosis
proliferation
prolonged transition
OPC apoptosis
Hypomyelination
MO necroptosis
Demyelination
myelin
proliferation
myelinating capacity
shortened transition
Hypomyelination & Working memory deficit
Normal myelin & Working memory deficit
energy support

Figure 7

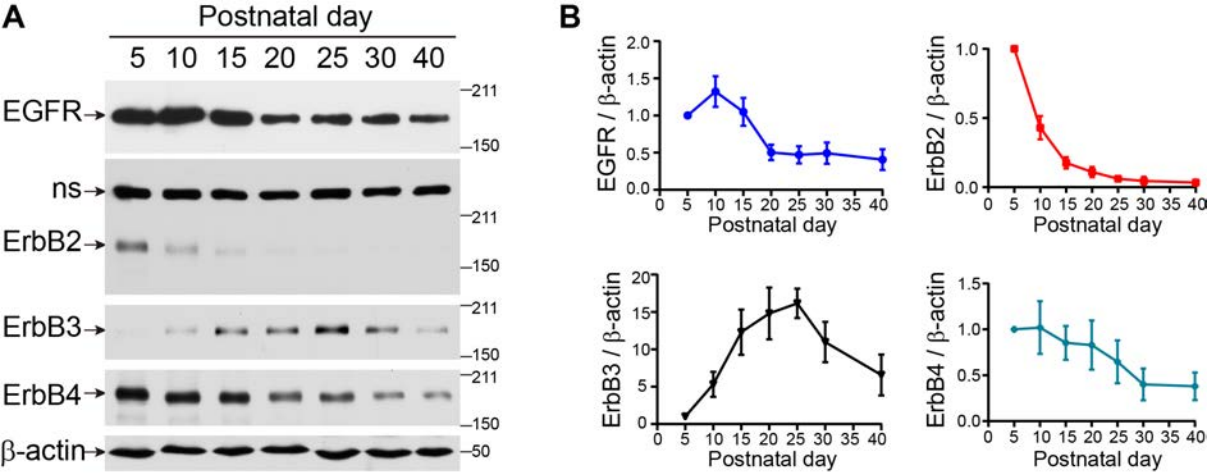

Figure 1- figure supplement 1

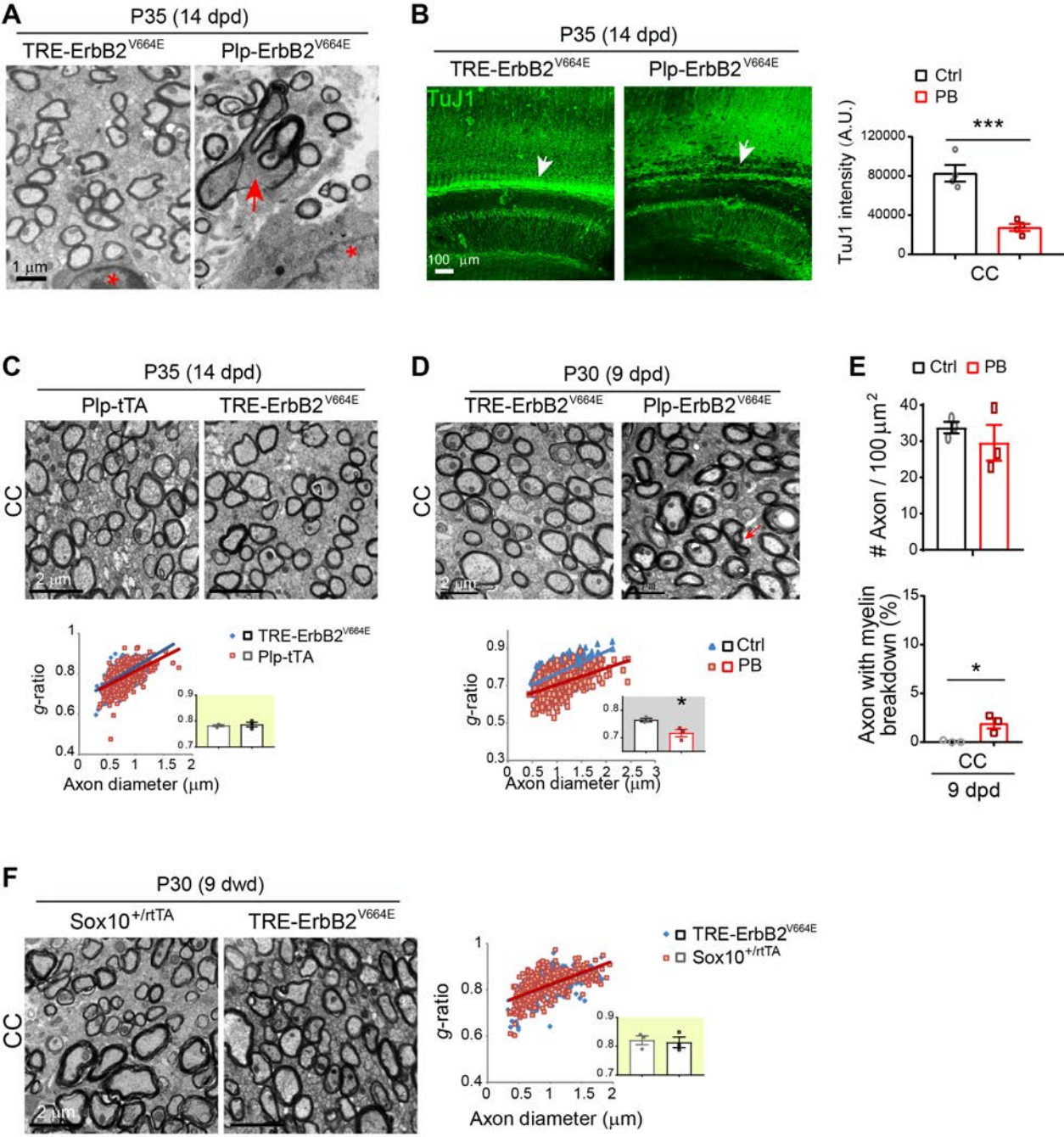

Figure 1- figure supplement 2

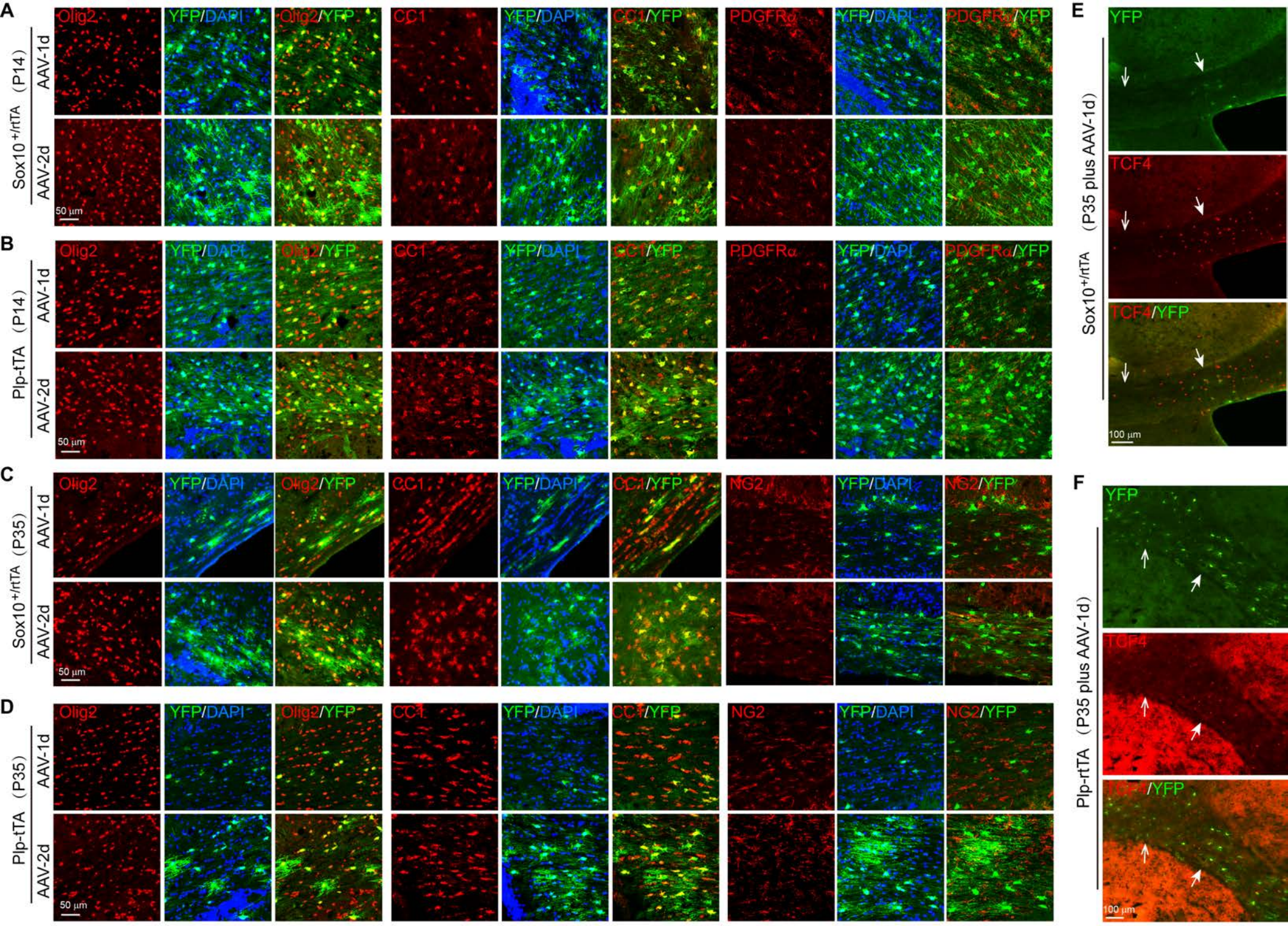

Figure 2- figure supplement 1

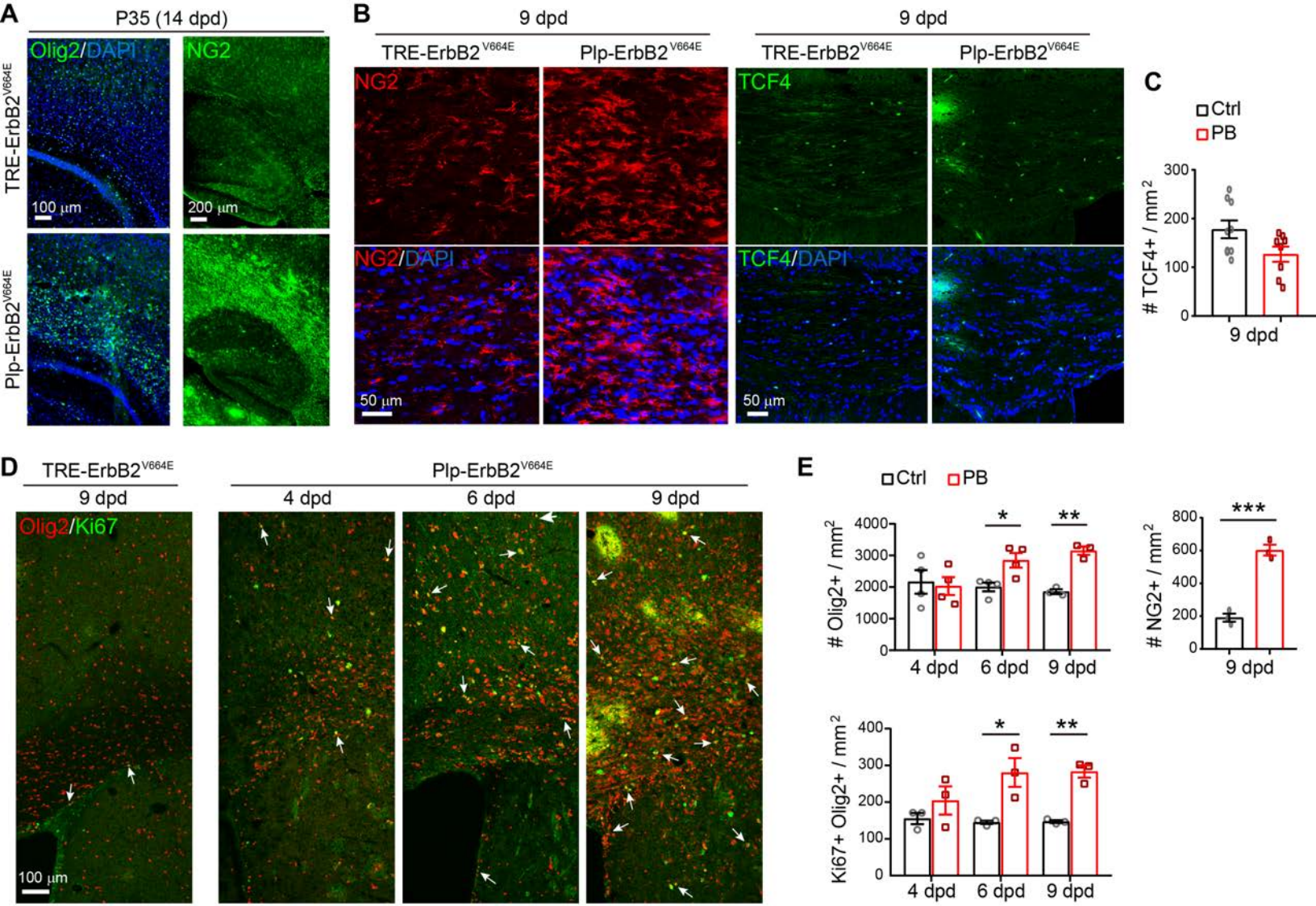

Figure 3- figure supplement 1

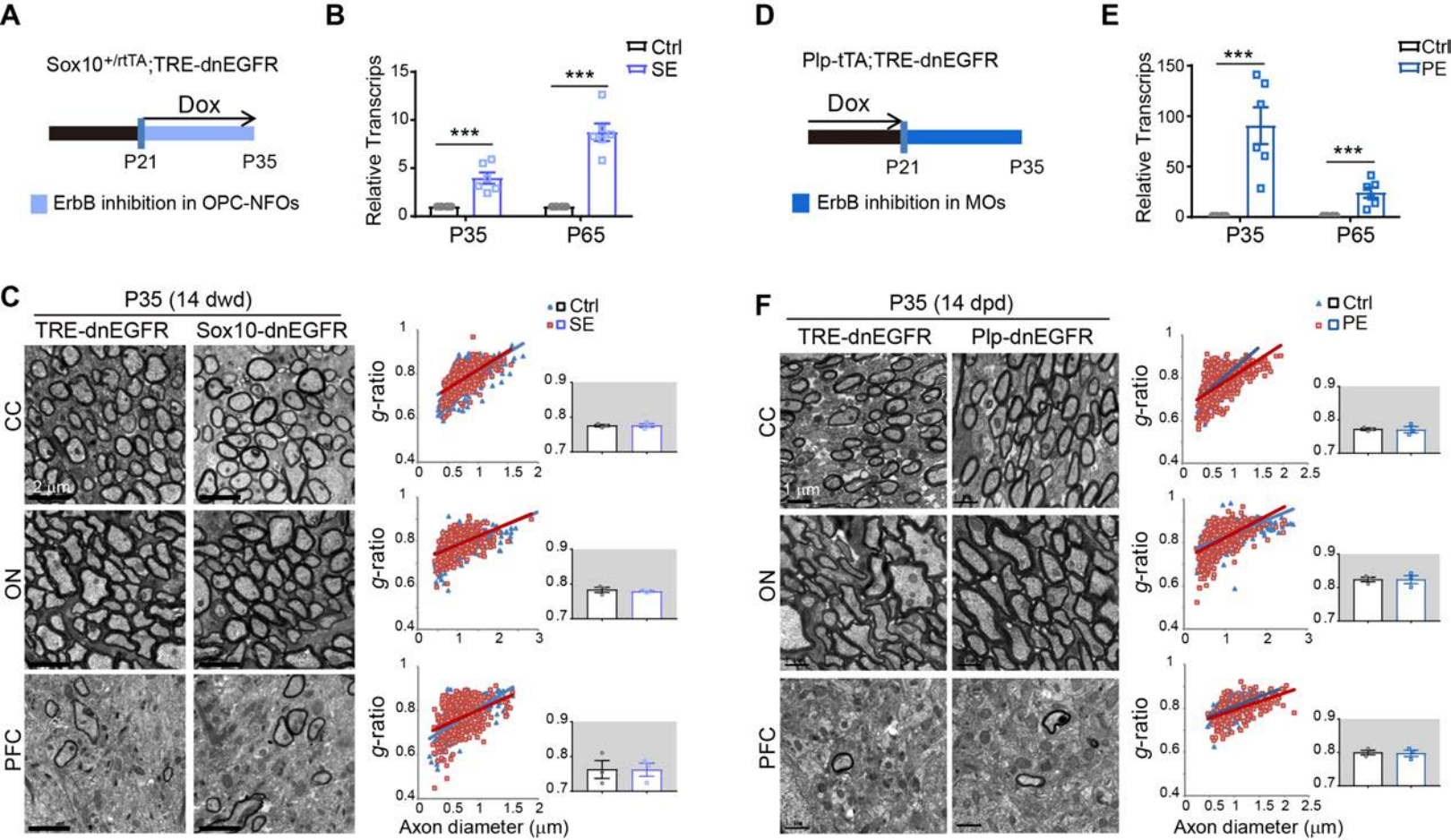

Figure 4- figure supplement 1

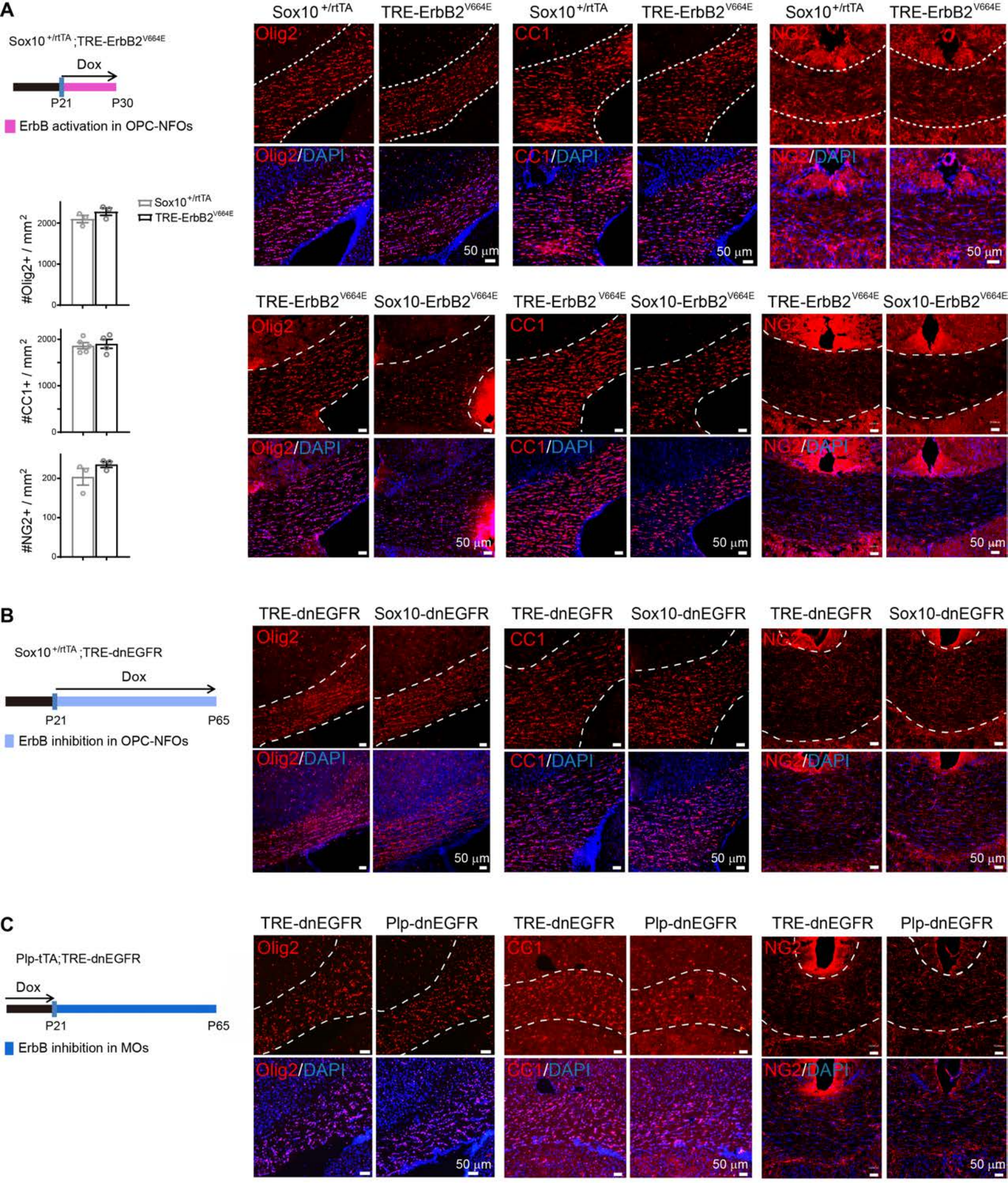

Figure 5- figure supplement 1

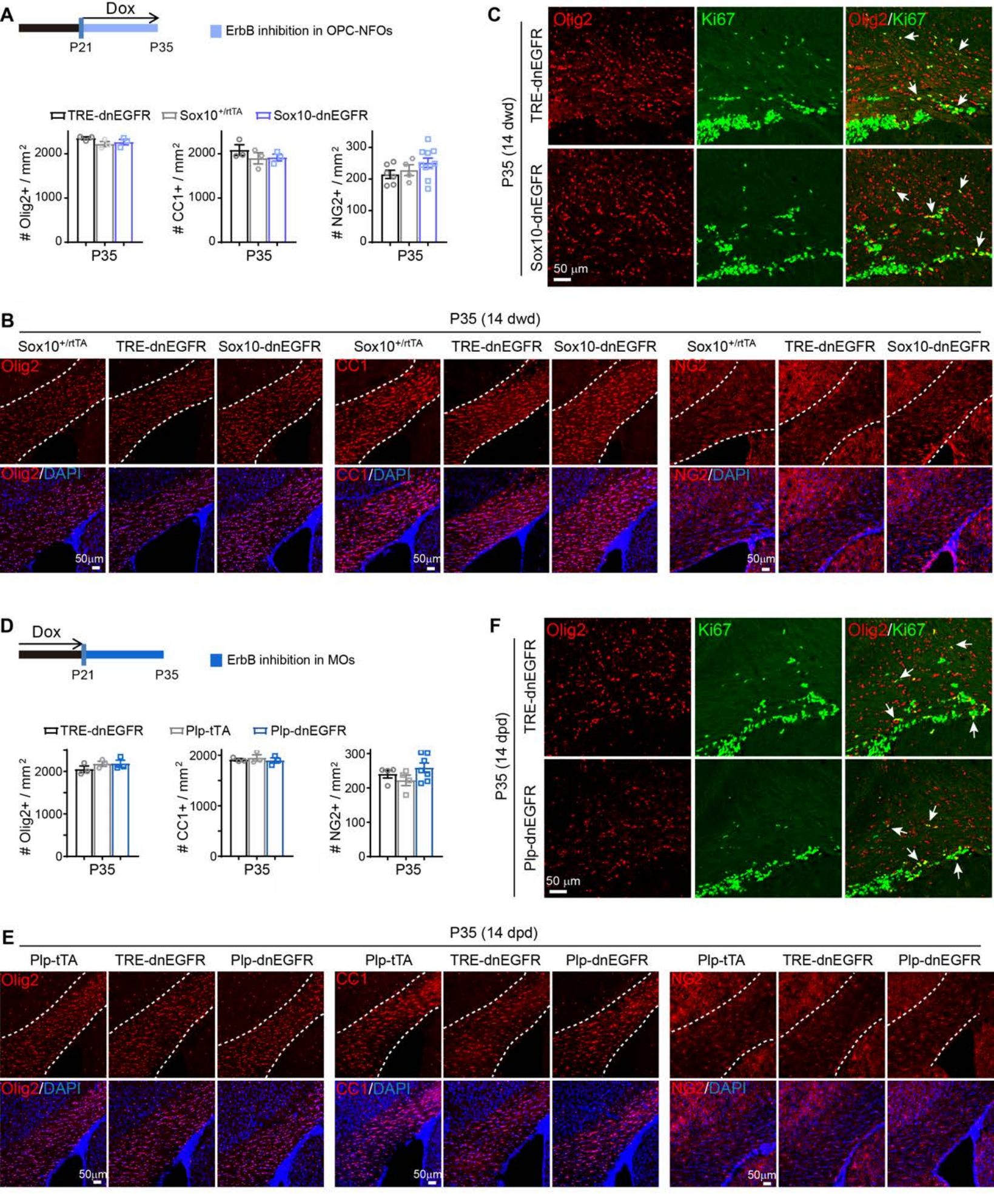

Figure 5- figure supplement 2

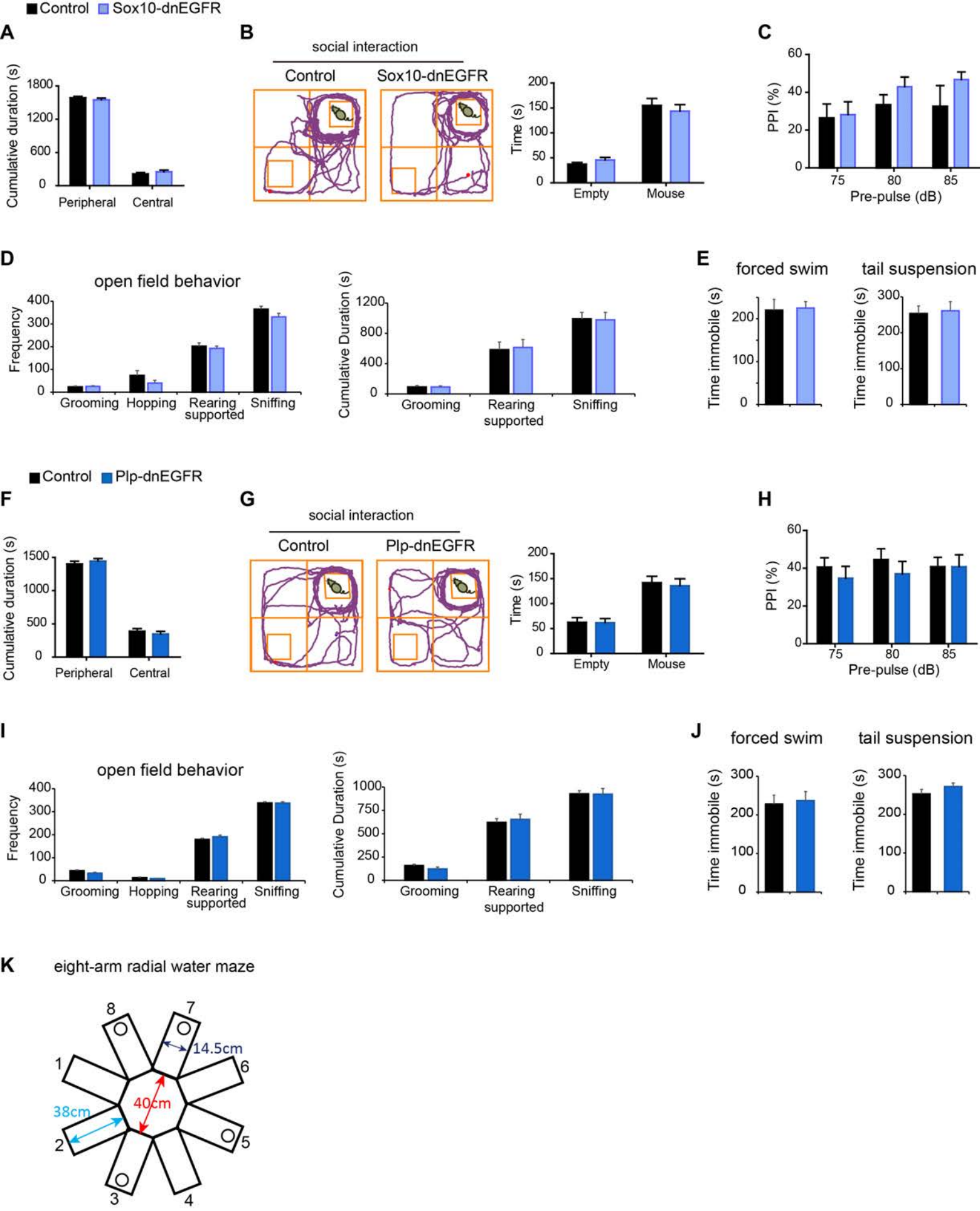

Figure 7- figure supplement 1